

RL-TR-97-151
In-House Report
JULY 1997



INCREMENTAL LENGTH DIFFRACTION COEFFICIENTS FOR THE SHADOW BOUNDARY OF A GENERAL CYLINDER

Thorkild B. Hansen and Robert A. Shore

APPROVED FOR PUBLIC RELEASE; DISTRIBUTION UNLIMITED.

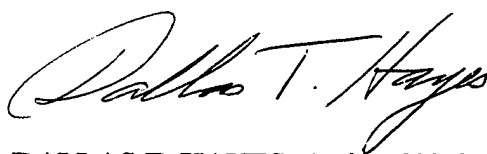
19980824 164

Rome Laboratory
Air Force Materiel Command
Rome, New York

This report has been reviewed by the Rome Laboratory Public Affairs Office (PA) and is releasable to the National Technical Information Service (NTIS). At NTIS it will be releasable to the general public, including foreign nations.

RL-TR-97-151 has been reviewed and is approved for publication.

APPROVED:



DALLAS T. HAYES, Acting Chief
Antennas and Components Division
Electromagnetics & Reliability Directorate

FOR THE COMMANDER:



HORST R. WITTMANN, Director
Electromagnetics & Reliability Directorate

If your address has changed or if you wish to be removed from the Rome Laboratory mailing list, or if the addressee is no longer employed by your organization, please notify Rome Laboratory/ERAA, Hanscom AFB, MA 01731. This will assist us in maintaining a current mailing list.

Do not return copies of this report unless contractual obligations or notices on a specific document require that it be returned.

REPORT DOCUMENTATION PAGE

Form Approved
OMB No. 0704-0188

Public reporting burden for this collection of information is estimated to average 1 hour per response, including the time for reviewing instructions, searching existing data sources, gathering and maintaining the data needed, and completing and reviewing the collection of information. Send comments regarding this burden estimate or any other aspect of this collection of information, including suggestions for reducing this burden, to Washington Headquarters Services, Directorate for Information Operations and Reports, 1215 Jefferson Davis Highway, Suite 1204, Arlington, VA 22202-4302, and to the Office of Management and Budget, Paperwork Reduction Project (0704-0188), Washington, DC 20503.

1. AGENCY USE ONLY (Leave blank)	2. REPORT DATE	3. REPORT TYPE AND DATES COVERED	
	July 1997	In-House Apr 94 - Mar 97	
4. TITLE AND SUBTITLE		5. FUNDING NUMBERS	
Incremental Length Diffraction Coefficients for the Shadow Boundary of a General Cylinder		PE 61102F PR 2304 TA I3 WU 02	
6. AUTHOR(S)			
Thorkild B. Hansen*, Robert A. Shore			
7. PERFORMING ORGANIZATION NAME(S) AND ADDRESS(ES)		8. PERFORMING ORGANIZATION REPORT NUMBER	
Rome Laboratory/ERAA 31 Grenier St Hanscom AFB, MA 01731-3010		RL-TR-97-151	
9. SPONSORING / MONITORING AGENCY NAME(S) AND ADDRESS(ES)		10. SPONSORING / MONITORING AGENCY REPORT NUMBER	
11. SUPPLEMENTARY NOTES			
Rome Laboratory Project Engineer: Robert A. Shore/ERAA, (781) 377-2058 *Subcontractor for CUBRC			
12a. DISTRIBUTION / AVAILABILITY STATEMENT		12b. DISTRIBUTION CODE	
Approved for public release; distribution unlimited.			
13. ABSTRACT (Maximum 200 words)			
<p>Incremental length diffraction coefficients (ILDCs) are obtained for the shadow boundaries of perfectly electrically conducting (PEC) convex cylinders of general cross-section. A two-step procedure is used. First, the nonuniform (NU) currents in the vicinity of the shadow boundary are approximated using Fock functions. The product of the approximated currents and the free-space Green's function is then integrated on a differential strip of the cylinder surface transverse to the shadow boundary to obtain the ILDCs. This integration is performed in closed form by employing quadratic polynomical approximations for the amplitude and unwrapped phase of the integrand. The current approximations are numerically verified for circular and parabolic cylinders. The integration procedure is numerically verified by demonstrating that it produces an accurate far-field pattern for a circular cylinder. Finally, as an example, the scattered far field of a PEC sphere is obtained by adding the integral of the NU ILDCs of a circular cylinder along the shadow boundary of the sphere to the physical optics (PO) far field of the sphere. This correction to the PO field is shown to significantly improve upon the accuracy of the PO far field approximation to the total scattered far field of the sphere.</p>			
14. SUBJECT TERMS		15. NUMBER OF PAGES	
Incremental length diffraction coefficients, Shadow boundary, Convex cylinder		38	
16. PRICE CODE			
17. SECURITY CLASSIFICATION OF REPORT	18. SECURITY CLASSIFICATION OF THIS PAGE	19. SECURITY CLASSIFICATION OF ABSTRACT	20. LIMITATION OF ABSTRACT
Unclassified	Unclassified	Unclassified	SAR

Contents

1	Introduction	1
2	Fock Currents on a Convex Cylinder	2
2.1	The Fock Current for TE Oblique Incidence	2
2.2	The Fock Current for TM Oblique Incidence	7
2.3	Examples	9
3	Integrating the Fock Currents to Obtain ILDC's	15
3.1	Quadratic Polynomial Approximations of the Amplitude and Phase of the ILDC Radiation Integral	16
3.2	Numerical Verification of the Quadratic Approximations	17
4	The Use of the ILDC's for a 3D Scatterer	24
4.1	Calculation of the Fields Scattered by a Sphere	25
5	Conclusions	26
References		29
Appendix	Closed-Form Expressions for an Integral	31

List of Figures

1	Cross section of a convex cylinder with smoothly varying radius of curvature.	3
2	Amplitude of $K_{\phi}^{TE,NU}(a, \phi, z)$ for circular cylinder, $ka = 60$, $\phi^i = 180^\circ$, $\theta^i = 90^\circ$. . .	10
3	Amplitude of $K_z^{TE,NU}(a, \phi, z)$ for a circular cylinder, $ka = 60$, $\phi^i = 180^\circ$, $\theta^i = 30^\circ$. .	11
4	Amplitude of $K_z^{TM,NU}(a, \phi, z)$ for a circular cylinder, $ka = 60$, $\phi^i = 180^\circ$, $\theta^i = 90^\circ$. .	12
5	Amplitude of $K_{\xi}^{TE,NU}(\phi_g, kh, z)$ for a parabolic cylinder, $kh = 60$, $\phi^i = 30^\circ$, $\theta^i = 90^\circ$. .	14
6	Amplitude of $K_z^{TE,NU}(\phi_g, kh, z)$ for a parabolic cylinder, $kh = 60$, $\phi^i = 30^\circ$, $\theta^i = 30^\circ$. .	14
7	Amplitude of $K_{\xi}^{TM,NU}(\phi_g, kh, z)$ for a parabolic cylinder, $kh = 60$, $\phi^i = 30^\circ$, $\theta^i = 90^\circ$. .	15
8	Circular cylinder illuminated by a TE plane wave	17
9	Amplitude of the exact nonuniform TE current on circular cylinder for $ka = 60$	18
10	Phase of the exact nonuniform TE current on circular cylinder for $ka = 60$	19
11	Exact values and quadratic approximation of $A(s)$ for $n = 6$, $\phi = 0^\circ$, and $ka = 60$. The endpoints are $s_j = \pi(j-1)/6$	19
12	Exact values and quadratic approximation of $P(s)$ for $n = 6$, $\phi = 0^\circ$, and $ka = 60$. The endpoints are $s_j = \pi(j-1)/6$	20
13	Exact values and quadratic approximation of $A(s)$ for $n = 6$, $\phi = 90^\circ$, and $ka = 60$. The endpoints are $s_j = \pi(j-1)/6$	20
14	Exact values and quadratic approximation of $P(s)$ for $n = 6$, $\phi = 90^\circ$, and $ka = 60$. The endpoints are $s_j = \pi(j-1)/6$	21
15	Exact values and quadratic approximation of $A(s)$ for $n = 6$, $\phi = 0^\circ$, and $ka = 60$. The endpoints are $s_1 = 0$, $s_2 = 60^\circ$, $s_3 = 80^\circ$, $s_4 = 90^\circ$, $s_5 = 105^\circ$, $s_6 = 135^\circ$, and $s_7 = 180^\circ$	21
16	Exact values and quadratic approximation of $P(s)$ for $n = 6$, $\phi = 0^\circ$, and $ka = 60$. The endpoints are $s_1 = 0$, $s_2 = 60^\circ$, $s_3 = 80^\circ$, $s_4 = 90^\circ$, $s_5 = 105^\circ$, $s_6 = 135^\circ$, and $s_7 = 180^\circ$	22
17	Exact and approximate NU TE far-field pattern for $ka = 60$ and $n = 4$, $n = 6$, and $n = 8$. The endpoints are $s_j = \pi(j-1)/n$; $0^\circ \leq \phi \leq 360^\circ$	22
18	Exact and approximate NU TE far-field pattern for $ka = 60$ and $n = 4$, $n = 6$, and $n = 8$. The endpoints are $s_j = \pi(j-1)/n$; $0^\circ \leq \phi \leq 110^\circ$	23
19	Three dimensional scatterer illuminated by a plane wave.	24
20	Amplitude of scattered H-plane far field of sphere, $ka = 60$, illuminated by a plane wave; $0^\circ \leq \theta \leq 180^\circ$	26
21	Amplitude of scattered H-plane far field of sphere, $ka = 60$, illuminated by a plane wave; $130^\circ \leq \theta \leq 180^\circ$	27

Acknowledgments

This work was supported by the Air Force Office of Scientific Research, Bolling AFB, DC.

Incremental Length Diffraction Coefficients for the Shadow Boundary of a General Cylinder

1 Introduction

In the physical theory of diffraction (PTD) [1], the scattered field is divided into a physical optics (PO) field and a nonuniform (NU) field. The PO field for perfectly electrically conducting (PEC) objects is obtained from an integration of the PO current over the object. One reason for the limited accuracy of the PO field is that the PO current fails to closely approximate the exact current in the vicinity of shadow boundaries and on the shadow side. A significant improvement in the accuracy of the computed fields can therefore be obtained by finding good approximations for the fields radiated by the NU currents near the shadow boundary. Approximations for these NU fields can be obtained by first integrating the product of the free-space Green's function and the approximated NU currents excited on a strip of differential width transverse to the shadow boundary of a canonical two-dimensional (2D) scatterer that closely conforms locally to the shape of the actual scatterer in the vicinity of the shadow boundary. The differential fields obtained by this integration are known as the incremental length diffraction coefficients (ILDC's). Once the ILDC's are determined, the NU fields are obtained by integrating them along the shadow boundary of the actual scatterer.

Although for some time ILDC's have been available for the shadow boundaries of two-dimensional (2D) PEC scatterers with sharp edges such as the wedge [2], [3], [4], [5] it is only recently that they have been obtained for convex, smoothly-curved cylinders. Hansen and Shore obtained ILDC's for the shadow boundary of a circular cylinder [6] and a parabolic cylinder [7] using an earlier form of the method of this report, and presented the basic ideas of this report in [8]. Yaghjian *et al.* [9] obtained shadow-boundary ILDC's for a convex cylinder by approximating the far fields radiated by the NU shadow-boundary currents of a convex cylinder by the far fields radiated by the NU shadow-boundary currents of circular cylinders, and then substituting the approximated fields into general expressions [5], [9], [10]. These approximate ILDC's were

then modified to account for a varying radius of curvature in the shadow region.

The purpose of this report is to show how ILDC's can be obtained for the NU currents near the shadow boundaries of PEC 2D convex cylinders of general cross-section and smoothly varying radius of curvature, by approximating and integrating the NU currents. We derive asymptotic expressions for the ILDC's that are rapidly calculable and usable in general-purpose computer codes. This method of obtaining convex-cylinder shadow-boundary ILDC's is an alternative to the field substitution of Yaghjian *et al.* [9] described above. The field substitution method, because it works directly with fields, is perhaps simpler than the method of this report. For applications in which heightened accuracy is important, however, the NU current approximation and integration method described here may be preferable because it yields more accurate ILDC's than does the field substitution method [11].

The report is organized as follows. In Section 2 we obtain the Fock approximations of the NU currents on a convex cylinder. These approximations are validated by specializing them to the cases of a circular and parabolic cylinder and showing that the Fock approximations to the NU currents closely match the exact NU currents. In Section 3 we show how the ILDC's corresponding to the Fock current approximations of Section 2 can be obtained efficiently by using an accurate and rapidly calculable approximation to the integral defining the ILDC. In Section 4 we show how to determine the canonical 2D cylinders from the actual 3D scatterers. As an example of obtaining and using shadow boundary ILDC's we show results obtained for the field scattered by a PEC sphere illuminated by a plane wave.

2 Fock Currents on a Convex Cylinder

We now derive simple expressions for the Fock currents [12] on a convex perfectly conducting cylinder illuminated by an obliquely incident plane wave (see Figure 1). These expressions are determined by applying the procedure in [13] to the Fock currents that are valid for normal incidence. The Fock currents for normal incidence are determined from expressions in [14]. Some of the results derived in this section are available in the literature, for example [15], [16, pp.83-86], and [14]. We note, however, that the Fock currents for oblique incidence in the illuminated region are given incorrectly in [15] and [14], and are not given in [16], and there are other errors as well. In the following derivations of the Fock current approximations, the cylinder axis is parallel to \hat{z} , and the unit normal vector for the cylinder is denoted \hat{n} . ρ_n denotes the radius of curvature of the curve that describes the cylinder cross-section in a plane perpendicular to \hat{z} , and it is assumed that ρ_n is a continuous function. The incident plane wave propagates in the direction \hat{k}^i . An $e^{-i\omega t}$ time dependence is assumed throughout with $\omega > 0$.

2.1 The Fock Current for TE Oblique Incidence

In this case the incident electric and magnetic plane-wave fields are given by

$$\mathbf{E}^{TE,i}(\mathbf{r}) = -Z_0 \hat{\phi}^i e^{i\mathbf{k}^i \cdot \mathbf{r}} \quad (1)$$

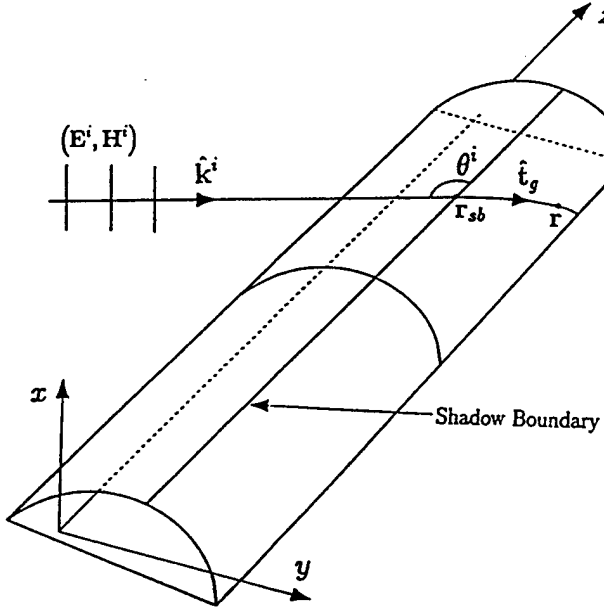


Figure 1: Cross section of a convex cylinder with smoothly varying radius of curvature.

and

$$\mathbf{H}^{TE,i}(\mathbf{r}) = -\hat{\theta}^i e^{i\mathbf{k}^i \cdot \mathbf{r}} \quad (2)$$

where Z_0 is the impedance of free space, $\mathbf{k}^i = k\hat{\mathbf{k}}^i$, and $\hat{\mathbf{k}}^i = -\hat{\mathbf{x}} \sin \theta^i \cos \phi^i - \hat{\mathbf{y}} \sin \theta^i \sin \phi^i - \hat{\mathbf{z}} \cos \theta^i$ is the propagation direction of the incident plane wave. Moreover, $\hat{\theta}^i$ and $\hat{\phi}^i$ are the spherical unit vectors corresponding to the direction (θ^i, ϕ^i) . We let $\mathbf{r} = x\hat{\mathbf{x}} + y\hat{\mathbf{y}} + z\hat{\mathbf{z}}$ denote a general point and let $\mathbf{r}_0 = x\hat{\mathbf{x}} + y\hat{\mathbf{y}}$ denote a point in the plane $z = 0$.

In the special case of normal incidence ($\theta^i = 90^\circ$) all fields are independent of z and the direction of propagation of the incident field is $\hat{\mathbf{k}}^i = \hat{\mathbf{k}}^{i,n} = -\hat{\mathbf{x}} \cos \phi^i - \hat{\mathbf{y}} \sin \phi^i$, so that the incident magnetic field is given by $\mathbf{H}^{TE,i,n}(\mathbf{r}_0) = \hat{\mathbf{z}} e^{i\mathbf{k}^{i,n} \cdot \mathbf{r}_0}$. The Fock current in the illuminated region can be written as [14, p.1666]

$$\mathbf{K}^{TE,n}(\mathbf{r}_0) = \hat{\mathbf{n}} \times \mathbf{H}^{TE,i,n}(\mathbf{r}_0) G \left(\left[\frac{k \rho_n(\mathbf{r}_0)}{2} \right]^{1/3} \hat{\mathbf{n}} \cdot \hat{\mathbf{k}}^{i,n} \right) \quad (3)$$

where $G(x) = e^{ix^3/3} g(x)$, with $g(x)$ being the Fock function defined in [17, pp. 63-64]. These Fock functions (as well as $f(x)$ and $F(x)$ defined below) are most easily obtained by interpolation of tabulated values for $|x| \leq 3$, and by use of asymptotic expressions for $|x| > 3$. Note that $\hat{\mathbf{n}} \times \mathbf{H}^{TE,i,n}(\mathbf{r}_0) = \hat{\mathbf{t}}_n e^{i\mathbf{k}^{i,n} \cdot \mathbf{r}_0}$, where $\hat{\mathbf{t}}_n$ is the tangent unit vector that is perpendicular to $\hat{\mathbf{z}}$ and satisfies $\hat{\mathbf{t}}_n = \hat{\mathbf{n}} \times \hat{\mathbf{z}}$. Since $\hat{\mathbf{n}} \times \mathbf{H}^{TE,i,n}(\mathbf{r}_0)$ is simply one half of the PO current at the point \mathbf{r}_0 , the Fock current (3) can also be written as

$$K_{t_n}^{TE,n}(\mathbf{r}_0) = \frac{1}{2} K_{t_n}^{TE,PO,n}(\mathbf{r}_0) G \left(\left[\frac{k \rho_n(\mathbf{r}_0)}{2} \right]^{1/3} \hat{\mathbf{n}} \cdot \hat{\mathbf{k}}^{i,n} \right). \quad (4)$$

Equation (4), valid for normal incidence, will now be used in conjunction with the procedure in [13] to obtain the Fock current for oblique incidence. According to [13, Eq.(13)], for oblique incidence the current can be expressed as

$$\mathbf{K}^{TE}(\mathbf{r}) = \left(\hat{\mathbf{t}}_n \sin \theta^i + \hat{\mathbf{z}} \frac{i \cos \theta^i}{k \sin \theta^i} \frac{\partial}{\partial t_n} \right) e^{-ikz \cos \theta^i} \left[K_{t_n}^{TE,n}(\mathbf{r}_0) \right]_{k \rightarrow k \sin \theta^i} \quad (5)$$

where $\left[K_{t_n}^{TE,n}(\mathbf{r}_0) \right]_{k \rightarrow k \sin \theta^i}$ indicates that k must be replaced by $k \sin \theta^i$ in the expression for $K_{t_n}^{n,TE}(\mathbf{r}_0)$. In [13] it is also shown that applying (5) to the PO current for normal incidence yields the PO current for oblique incidence. Thus, by applying (5) to (4) we obtain the following expression for the Fock current for oblique incidence

$$\begin{aligned} \mathbf{K}^{TE}(\mathbf{r}) = & \frac{1}{2} \mathbf{K}^{TE,PO}(\mathbf{r}) \left[G \left(\left[\frac{k \rho_n(\mathbf{r}_0)}{2} \right]^{1/3} \hat{\mathbf{n}} \cdot \hat{\mathbf{k}}^{i,n} \right) \right]_{k \rightarrow k \sin \theta^i} \\ & + \hat{\mathbf{z}} \frac{i \cos \theta^i}{2k \sin \theta^i} e^{-ikz \cos \theta^i} \left[K_{t_n}^{TE,PO,n}(\mathbf{r}_0) \frac{\partial}{\partial t_n} G \left(\left[\frac{k \rho_n(\mathbf{r}_0)}{2} \right]^{1/3} \hat{\mathbf{n}} \cdot \hat{\mathbf{k}}^{i,n} \right) \right]_{k \rightarrow k \sin \theta^i} \end{aligned} \quad (6)$$

where $\mathbf{K}^{TE,PO}(\mathbf{r}) = 2 \hat{\mathbf{n}} \times \mathbf{H}^{TE,i}(\mathbf{r})$ is the PO current for oblique incidence. Using the relation $\frac{\partial}{\partial t_n} \hat{\mathbf{n}} \cdot \hat{\mathbf{k}}^{i,n} = \hat{\mathbf{k}}^{i,n} \cdot \hat{\mathbf{t}}_n / \rho_n$, one finds that for large $k \rho_n$ the second term of (6) is negligible compared to the first term of (6). Since $\sin \theta^i \hat{\mathbf{n}} \cdot \hat{\mathbf{k}}^{i,n} = \hat{\mathbf{n}} \cdot \hat{\mathbf{k}}^i$, we find that

$$\left[\left(\frac{k \rho_n(\mathbf{r}_0)}{2} \right)^{1/3} \hat{\mathbf{n}} \cdot \hat{\mathbf{k}}^{i,n} \right]_{k \rightarrow k \sin \theta^i} = \left(\frac{k \rho_g(\mathbf{r})}{2} \right)^{1/3} \hat{\mathbf{n}} \cdot \hat{\mathbf{k}}^i \quad (7)$$

where

$$\rho_g(\mathbf{r}) = \frac{\rho_n(\mathbf{r}_0)}{\sin^2 \theta^i} \quad (8)$$

is the radius of curvature of the geodesic that forms the angle θ^i with the z axis. Consequently, in the illuminated region, the Fock current for oblique incidence is given by

$$\mathbf{K}^{TE}(\mathbf{r}) = \hat{\mathbf{n}} \times \mathbf{H}^{TE,i}(\mathbf{r}) G \left(\left[\frac{k \rho_g(\mathbf{r})}{2} \right]^{1/3} \hat{\mathbf{n}} \cdot \hat{\mathbf{k}}^i \right). \quad (9)$$

The total current approximated in (9) is the sum of the PO current and the nonuniform (NU) current. By defining the modified Fock function

$$\tilde{G}(x) = G(x) - 2 \quad (10)$$

and using \tilde{G} instead of G in (9) we obtain the Fock current approximation for the TE NU current in the illuminated region

$$\mathbf{K}^{TE,NU}(\mathbf{r}) = \hat{\mathbf{n}} \times \mathbf{H}^{TE,i}(\mathbf{r}) \tilde{G} \left(\left[\frac{k \rho_g(\mathbf{r})}{2} \right]^{1/3} \hat{\mathbf{n}} \cdot \hat{\mathbf{k}}^i \right). \quad (11)$$

Since $\hat{\mathbf{n}} \cdot \hat{\mathbf{k}}^i = 0$ everywhere on the shadow boundary, the Fock current at the point \mathbf{r}_{sb} on the shadow boundary is

$$\mathbf{K}^{TE}(\mathbf{r}_{sb}) = \hat{\mathbf{n}}_{sb} \times \mathbf{H}^{TE,i}(\mathbf{r}_{sb})G(0). \quad (12)$$

The asymptotic formula

$$G(x) = 2 + \frac{i}{2x^3} + O(x^{-6}), \quad x \rightarrow -\infty \quad (13)$$

shows that in the illuminated region far from the shadow boundary the Fock current is

$$\mathbf{K}^{TE}(\mathbf{r}) = 2 \hat{\mathbf{n}} \times \mathbf{H}^{TE,i}(\mathbf{r}) + i \frac{\hat{\mathbf{n}} \times \mathbf{H}^{TE,i}(\mathbf{r})}{k\rho_g(\mathbf{r})(\hat{\mathbf{n}} \cdot \hat{\mathbf{k}}^i)^3} + O\left(\frac{1}{[k\rho_g(\mathbf{r})]^2(\hat{\mathbf{n}} \cdot \hat{\mathbf{k}}^i)^6}\right). \quad (14)$$

In (14) the first term is the PO current and the second term is the first higher-order optics term.

Now consider the Fock current on the shadow side of the cylinder. For normal incidence the formulas of [14, p. 1666] show that the Fock current is

$$\mathbf{K}^{TE,n}(\mathbf{r}_0) = Y_0 \hat{\mathbf{n}}_{sb} \cdot \mathbf{E}^{TE,i,n}(\mathbf{r}_{sb0}) e^{ik s_n(\mathbf{r}_0)} g(x_n) \left(\frac{\rho_n(\mathbf{r}_{sb0})}{\rho_n(\mathbf{r}_0)} \right)^{1/6} \hat{\mathbf{t}}_n \quad (15)$$

where \mathbf{r}_{sb0} is the point of the shadow boundary that lies in the $z = 0$ plane, $Y_0 = 1/Z_0$ is the admittance of free space, $\hat{\mathbf{n}}_{sb}$ is the normal at the shadow boundary, $s_n(\mathbf{r}_0)$ is the distance along the cylinder from the point \mathbf{r}_{sb0} on the shadow boundary to the point \mathbf{r}_0 , and

$$x_n = \left(\frac{k}{2} \right)^{1/3} \int_{\mathbf{r}_{sb0}}^{\mathbf{r}_0} \frac{ds_n}{\rho_n(s_n)^{2/3}}, \quad (16)$$

is the Fock parameter (the integration in (16) is *on* the surface of the cylinder). Moreover, $\hat{\mathbf{t}}_n$ is that unit tangent vector to the cylinder which is perpendicular to $\hat{\mathbf{z}}$ and is equal to $\hat{\mathbf{k}}^{i,n}$ at the shadow boundary. On the illuminated side the unit tangent vector was defined as $\hat{\mathbf{t}}_n = \hat{\mathbf{n}} \times \hat{\mathbf{z}}$, and the two unit tangent vectors on either side of the shadow boundary are therefore not always equal at the shadow boundary (in some cases they are opposite). However, the unit tangent vector in the illuminated region was used only in intermediate steps of the derivation, and it does not appear in any of the final formulas for the current in the illuminated region. Note also that $Y_0 \hat{\mathbf{n}}_{sb} \cdot \mathbf{E}^{TE,i,n}(\mathbf{r}_{sb0}) = \pm e^{i\mathbf{k}^{i,n} \cdot \mathbf{r}_{sb0}}$ since the incident electric field is always parallel to the normal at the shadow boundary.

To obtain the Fock current for oblique incidence, we insert (15) into (5) and note that (5) remains unchanged when $\hat{\mathbf{t}}_n$ is reversed. It is found that for large $k\rho_n$, the terms involving the derivative of $g(x_n)$ or the derivative of $[\rho_n(\mathbf{r}_{sb0})/\rho_n(\mathbf{r}_0)]^{1/6}$ are negligible compared to the two other terms that result when (15) is inserted into (5). Thus, we have

$$\begin{aligned} \mathbf{K}^{TE}(\mathbf{r}) = Y_0 e^{-ikz \cos \theta^i} & \left[\hat{\mathbf{n}}_{sb} \cdot \mathbf{E}^{TE,i,n}(\mathbf{r}_{sb0}) \right]_{k \rightarrow k \sin \theta^i} \left(\frac{\rho_n(\mathbf{r}_{sb0})}{\rho_n(\mathbf{r}_0)} \right)^{1/6} g([x_n]_{k \rightarrow k \sin \theta^i}) \\ & \left(\hat{\mathbf{t}}_n \sin \theta^i e^{ik \sin \theta^i s_n(\mathbf{r}_0)} + \hat{\mathbf{z}} \frac{i \cos \theta^i}{k \sin \theta^i} \frac{\partial}{\partial t_n} e^{ik \sin \theta^i s_n(\mathbf{r}_0)} \right). \end{aligned} \quad (17)$$

The last factor in (17) simply equals $(\hat{\mathbf{t}}_n \sin \theta^i - \hat{\mathbf{z}} \cos \theta^i) e^{ik \sin \theta^i s_n(\mathbf{r}_0)} = \hat{\mathbf{t}}_g e^{ik \sin \theta^i s_n(\mathbf{r}_0)}$, where $\hat{\mathbf{t}}_g$ is the tangent along the geodesic that forms the angle θ^i with the z axis, as shown in Figure 1. By unrolling the cylinder one finds that $\sin \theta^i s_n(\mathbf{r}_0) - \cos \theta^i (z - z_{sb}) = s_g(\mathbf{r})$, where $s_g(\mathbf{r})$ is the distance along the geodesic from the point $\mathbf{r}_{sb} = x_{sb}\hat{\mathbf{x}} + y_{sb}\hat{\mathbf{y}} + z_{sb}\hat{\mathbf{z}}$ on the shadow boundary to the point \mathbf{r} in the shadow region. Thus,

$$e^{-ikz \cos \theta^i} \left[e^{ik s_n(\mathbf{r}_0)} e^{i\mathbf{k}^i \cdot \mathbf{r}_{sb0}} \right]_{k \rightarrow k \sin \theta^i} = e^{ik s_g(\mathbf{r})} e^{i\mathbf{k}^i \cdot \mathbf{r}_{sb}} \quad (18)$$

showing that

$$e^{-ikz \cos \theta^i} e^{ik \sin \theta^i s_n(\mathbf{r}_0)} \left[\hat{\mathbf{n}}_{sb} \cdot \mathbf{E}^{TE,i,n}(\mathbf{r}_{sb0}) \right]_{k \rightarrow k \sin \theta^i} = \hat{\mathbf{n}}_{sb} \cdot \mathbf{E}^{TE,i}(\mathbf{r}_{sb}) e^{ik s_g(\mathbf{r})}. \quad (19)$$

From the relation (8) between ρ_n and ρ_g and the formula $ds_n = \sin \theta^i ds_g$ we find that $[x_n]_{k \rightarrow k \sin \theta^i}$ simply equals

$$x_g = \left(\frac{k}{2} \right)^{1/3} \int_{\mathbf{r}_{sb}}^{\mathbf{r}} \frac{ds_g}{\rho_g(s_g)^{2/3}} \quad (20)$$

where the integration is performed along the geodesic that starts at \mathbf{r}_{sb} and ends at the point \mathbf{r} in the shadow region. Inserting all these results into (17) proves that the Fock current in the shadow region is given by

$$\mathbf{K}^{TE}(\mathbf{r}) = Y_0 \hat{\mathbf{n}}_{sb} \cdot \mathbf{E}^{TE,i}(\mathbf{r}_{sb}) e^{ik s_g(\mathbf{r})} g(x_g) \left(\frac{\rho_g(\mathbf{r}_{sb})}{\rho_g(\mathbf{r})} \right)^{1/6} \hat{\mathbf{t}}_g \quad (21)$$

when the incident field is the plane wave in (1) and (2).

At the shadow boundary the expression in (21) reduces to

$$\mathbf{K}^{TE}(\mathbf{r}_{sb}) = Y_0 \hat{\mathbf{n}}_{sb} \cdot \mathbf{E}^{TE,i}(\mathbf{r}_{sb}) g(0) \hat{\mathbf{k}}^i \quad (22)$$

which can be shown to be in agreement with (12) by use of $g(0) = G(0)$, $\hat{\phi}^i = \hat{\mathbf{n}}_{sb}$ or $\hat{\phi}^i = -\hat{\mathbf{n}}_{sb}$, and $\hat{\mathbf{t}}_{g,sb} = \hat{\mathbf{k}}^i$. For large positive values of its argument the Fock function $g(x)$ is given by [17, p. 64]

$$g(x) \sim \frac{e^{\beta_1 x e^{5i\pi/6}}}{\beta_1 Ai(-\beta_1)}, \quad x \rightarrow +\infty, \quad (23)$$

where β_1 is the negative of the first zero of the derivative of the Airy function. Substituting (23) into (21) gives us the first creeping wave on the convex cylinder

$$\mathbf{K}^{TE}(\mathbf{r}) \sim Y_0 \hat{\mathbf{n}}_{sb} \cdot \mathbf{E}^{TE,i}(\mathbf{r}_{sb}) e^{ik s_g(\mathbf{r})} \frac{e^{\beta_1 x_g e^{5i\pi/6}}}{\beta_1 Ai(-\beta_1)} \left(\frac{\rho_g(\mathbf{r}_{sb})}{\rho_g(\mathbf{r})} \right)^{1/6} \hat{\mathbf{t}}_g. \quad (24)$$

2.2 The Fock Current for TM Oblique Incidence

In this case the incident electric and magnetic plane-wave fields are given by

$$\mathbf{E}^{TM,i}(\mathbf{r}) = -\hat{\theta}^i e^{i\mathbf{k}^i \cdot \mathbf{r}} \quad (25)$$

and

$$\mathbf{H}^{TM,i}(\mathbf{r}) = Y_0 \hat{\phi}^i e^{i\mathbf{k}^i \cdot \mathbf{r}} \quad (26)$$

where Y_0 is the impedance of free space. For normal incidence the electric field in (25) is given by $\mathbf{E}^{TM,i,n}(\mathbf{r}_0) = \hat{\mathbf{z}} e^{i\mathbf{k}^{i,n} \cdot \mathbf{r}_0}$, and [14, p.1666] shows that the Fock approximation to the total current on the illuminated side of the cylinder is

$$K_z^{TM,n}(\mathbf{r}_0) = iY_0 \hat{\mathbf{z}} \cdot \mathbf{E}^{TM,i,n}(\mathbf{r}_0) F\left(\left[\frac{k\rho_n(\mathbf{r}_0)}{2}\right]^{1/3} \hat{\mathbf{n}} \cdot \hat{\mathbf{k}}^{i,n}\right) \left[\frac{k\rho_n(\mathbf{r}_0)}{2}\right]^{-1/3} \quad (27)$$

where $F(x) = e^{ix^3/3} f(x)$ and $f(x)$ is the Fock function defined in [17, pp. 63-64]. Since the PO current for normal incidence is

$$\mathbf{K}^{TM,PO,n}(\mathbf{r}_0) = 2 \hat{\mathbf{n}} \times \mathbf{H}^{TM,i,n}(\mathbf{r}_0) = -2Y_0 \hat{\mathbf{n}} \cdot \hat{\mathbf{k}}^{i,n} e^{i\mathbf{k}^{i,n} \cdot \mathbf{r}_0} \hat{\mathbf{z}} \quad (28)$$

we can write the Fock current (27) as

$$\begin{aligned} \mathbf{K}^{TM,n}(\mathbf{r}_0) &= \hat{\mathbf{z}} K_z^{TM,n}(\mathbf{r}_0) \\ &= -\frac{i}{2} \mathbf{K}^{TM,PO,n}(\mathbf{r}_0) F\left(\left[\frac{k\rho_n(\mathbf{r}_0)}{2}\right]^{1/3} \hat{\mathbf{n}} \cdot \hat{\mathbf{k}}^{i,n}\right) \left(\left[\frac{k\rho_n(\mathbf{r}_0)}{2}\right]^{1/3} \hat{\mathbf{n}} \cdot \hat{\mathbf{k}}^{i,n}\right)^{-1}. \end{aligned} \quad (29)$$

According to [13] the current for oblique incidence can be determined from the current for normal incidence through the equation

$$K_z^{TM}(\mathbf{r}) = e^{-ikz \cos \theta^i} \left[K_z^{TM,n}(\mathbf{r}_0) \right]_{k \rightarrow k \sin \theta^i} \quad (30)$$

and in [13] it is also shown that applying (30) to the PO current for normal incidence yields the PO current for oblique incidence. Inserting the Fock current (29) into (30) shows that the Fock current for oblique incidence is

$$\mathbf{K}^{TM}(\mathbf{r}) = \hat{\mathbf{z}} K_z^{TM}(\mathbf{r}) = -i \hat{\mathbf{n}} \times \mathbf{H}^{TM,i}(\mathbf{r}) F\left(\left(\frac{k\rho_g(\mathbf{r})}{2}\right)^{1/3} \hat{\mathbf{n}} \cdot \hat{\mathbf{k}}^i\right) \left(\left[\frac{k\rho_g(\mathbf{r})}{2}\right]^{1/3} \hat{\mathbf{n}} \cdot \hat{\mathbf{k}}^i\right)^{-1} \quad (31)$$

where we have used (7) and inserted the expression $\mathbf{K}^{TM,PO}(\mathbf{r}) = 2 \hat{\mathbf{n}} \times \mathbf{H}^{TM,i}(\mathbf{r})$ for the PO current. Alternatively, we can insert the Fock current (27) into (30) to get

$$K_z^{TM}(\mathbf{r}) = \frac{iY_0}{\sin^2 \theta^i} \hat{\mathbf{z}} \cdot \mathbf{E}^{TM,i}(\mathbf{r}) F\left(\left[\frac{k\rho_g(\mathbf{r})}{2}\right]^{1/3} \hat{\mathbf{n}} \cdot \hat{\mathbf{k}}^i\right) \left[\frac{k\rho_g(\mathbf{r})}{2}\right]^{-1/3} \quad (32)$$

where we have used the formula

$$e^{-ikz \cos \theta^i} \left[\hat{\mathbf{z}} \cdot \mathbf{E}^{TM,i,n}(\mathbf{r}_0) \right]_{k \rightarrow k \sin \theta^i} = \frac{\hat{\mathbf{z}} \cdot \mathbf{E}^{TM,i}(\mathbf{r})}{\sin \theta^i}. \quad (33)$$

Since the total current approximated in (31) or (32) is the sum of the PO current and the NU current, by defining the modified Fock function

$$\tilde{F}(x) = F(x) - 2ix \quad (34)$$

and using \tilde{F} instead of F in (31) or (32) we obtain the Fock current approximation for the TM NU current in the illuminated region

$$\begin{aligned} \mathbf{K}^{TM,NU}(\mathbf{r}) &= \hat{\mathbf{z}} K_z^{TM,NU}(\mathbf{r}) \\ &= -i \hat{\mathbf{n}} \times \mathbf{H}^{TM,i}(\mathbf{r}) \tilde{F} \left(\left[\frac{k \rho_g(\mathbf{r})}{2} \right]^{1/3} \hat{\mathbf{n}} \cdot \hat{\mathbf{k}}^i \right) \left(\left[\frac{k \rho_g(\mathbf{r})}{2} \right]^{1/3} \hat{\mathbf{n}} \cdot \hat{\mathbf{k}}^i \right)^{-1} \end{aligned} \quad (35)$$

or

$$K_z^{TM,NU}(\mathbf{r}) = \frac{i Y_0}{\sin^2 \theta^i} \hat{\mathbf{z}} \cdot \mathbf{E}^{TM,i}(\mathbf{r}) \tilde{F} \left(\left[\frac{k \rho_g(\mathbf{r})}{2} \right]^{1/3} \hat{\mathbf{n}} \cdot \hat{\mathbf{k}}^i \right) \left[\frac{k \rho_g(\mathbf{r})}{2} \right]^{-1/3}. \quad (36)$$

At a point \mathbf{r}_{sb} on the shadow boundary both $\hat{\mathbf{n}} \cdot \hat{\mathbf{k}}^i$ and $\hat{\mathbf{n}} \times \mathbf{H}^{TM,i}$ equal zero, and we find that

$$\frac{\hat{\mathbf{n}} \times \mathbf{H}^{TM,i}(\mathbf{r})}{\hat{\mathbf{n}} \cdot \hat{\mathbf{k}}^i} \rightarrow -\frac{Y_0 e^{i\hat{\mathbf{k}}^i \cdot \mathbf{r}_{sb}}}{\sin \theta^i} \hat{\mathbf{z}} = -\frac{\hat{\mathbf{n}}_{sb} \cdot \mathbf{H}^{TM,i}(\mathbf{r}_{sb})}{\hat{\mathbf{n}}_{sb} \cdot \hat{\phi}^i \sin \theta^i} \hat{\mathbf{z}}, \quad \mathbf{r} \rightarrow \mathbf{r}_{sb} \quad (37)$$

so that the Fock current (31) at the shadow boundary becomes

$$\mathbf{K}^{TM}(\mathbf{r}_{sb}) = \hat{\mathbf{z}} K_z^{TM}(\mathbf{r}_{sb}) = \hat{\mathbf{z}} \frac{i F(0) \hat{\mathbf{n}}_{sb} \cdot \mathbf{H}^{TM,i}(\mathbf{r}_{sb})}{\hat{\mathbf{n}}_{sb} \cdot \hat{\phi}^i \sin \theta^i} \left(\frac{k \rho_g(\mathbf{r}_{sb})}{2} \right)^{-1/3} \quad (38)$$

which is seen from the plane-wave expressions (25) and (26) to agree with the result obtained from (32).

For large negative values of its argument, the function $F(x)$ is given by [17, p. 64]

$$F(x) \sim 2ix + \frac{1}{2x^2} + O(x^{-5}), \quad x \rightarrow -\infty, \quad (39)$$

so that the current in the illuminated region away from the shadow boundary is

$$\mathbf{K}^{TM}(\mathbf{r}) \sim 2 \hat{\mathbf{n}} \times \mathbf{H}^{TM,i}(\mathbf{r}) - i \frac{\hat{\mathbf{n}} \times \mathbf{H}^{TM,i}(\mathbf{r})}{k \rho_g(\mathbf{r}) (\hat{\mathbf{n}} \cdot \hat{\mathbf{k}}^i)^3} + O \left(\frac{1}{(k \rho_g)^2 (\hat{\mathbf{n}} \cdot \hat{\mathbf{k}}^i)^6} \right) \quad (40)$$

in which the first term is the PO current and the second term is the first higher-order optics term.

On the shadow side of the cylinder, the Fock approximation for normal incidence to the total current is [14, p. 1666]

$$K_z^{TM,n}(\mathbf{r}_0) = i f(x_n) e^{ik s_n(\mathbf{r}_0)} \frac{\hat{\mathbf{n}}_{sb} \cdot \mathbf{H}^{TM,i,n}(\mathbf{r}_{sb0})}{\hat{\mathbf{n}}_{sb} \cdot \hat{\phi}^i} \left(\frac{\rho_n(\mathbf{r}_{sb0})}{\rho_n(\mathbf{r}_0)} \right)^{1/6} \left(\frac{k \rho_n(\mathbf{r}_0)}{2} \right)^{-1/3} \quad (41)$$

where the Fock parameter x_n is defined in (16). Inserting (41) into (30), and using (18), we find that the Fock current for oblique incidence is

$$K_z^{TM}(\mathbf{r}) = i f(x_g) e^{ik s_g(\mathbf{r})} \frac{\hat{\mathbf{n}}_{sb} \cdot \mathbf{H}^{TM,i}(\mathbf{r}_{sb})}{\hat{\mathbf{n}}_{sb} \cdot \hat{\phi}^i \sin \theta^i} \left(\frac{\rho_g(\mathbf{r}_{sb})}{\rho_g(\mathbf{r})} \right)^{1/6} \left(\frac{k \rho_g(\mathbf{r})}{2} \right)^{-1/3} \quad (42)$$

with x_g given by (20).

At the shadow boundary, the value of the Fock current (42) is

$$K_z^{TM}(\mathbf{r}_{sb}) = i f(0) \frac{\hat{\mathbf{n}}_{sb} \cdot \mathbf{H}^{TM,i}(\mathbf{r}_{sb})}{\hat{\mathbf{n}}_{sb} \cdot \hat{\phi}^i \sin \theta^i} \left(\frac{k \rho_g(\mathbf{r}_{sb})}{2} \right)^{-1/3} \quad (43)$$

which agrees with the result in (38) because $f(0) = F(0)$. For large positive values of its argument, the Fock function $f(x)$ is given by [17, p. 64]

$$f(x) \sim \frac{e^{-i\pi/3} e^{\alpha_1 x e^{5i\pi/6}}}{Ai'(-\alpha_1)}, \quad x \rightarrow +\infty, \quad (44)$$

where α_1 is the negative of the first zero of the Airy function. Substituting (44) into (42) gives the first creeping wave on the convex cylinder

$$K_z^{TM}(\mathbf{r}) \sim i \frac{e^{-i\pi/3} e^{\alpha_1 x_g e^{5i\pi/6}} e^{ik s_g(\mathbf{r})}}{Ai'(-\alpha_1)} \frac{\hat{\mathbf{n}}_{sb} \cdot \mathbf{H}^{TM,i}(\mathbf{r}_{sb})}{\hat{\mathbf{n}}_{sb} \cdot \hat{\phi}^i \sin \theta^i} \left(\frac{\rho_g(\mathbf{r}_{sb})}{\rho_g(\mathbf{r})} \right)^{1/6} \left(\frac{k \rho_g(\mathbf{r})}{2} \right)^{-1/3}. \quad (45)$$

2.3 Examples

We now specialize the Fock current approximations for a general convex PEC cylinder obtained above to the cases of a circular and parabolic cylinder. Consider first a circular cylinder of radius a illuminated by the TE plane wave given by (1) and (2). For the Fock current approximation to the TE NU current in the illuminated region we obtain from (11)

$$\begin{aligned} \mathbf{K}^{TE,NU}(a, \phi, z) \approx & \left[-\hat{\phi} \sin \theta^i + \hat{z} \cos \theta^i \sin(\phi - \phi^i) \right] e^{-ika \sin \theta^i \cos(\phi - \phi^i)} e^{-ikz \cos \theta^i} \\ & \cdot \tilde{G} \left[-\left(\frac{ka \sin \theta^i}{2} \right)^{1/3} \cos(\phi - \phi^i) \right], \quad |\phi - \phi^i| < \pi/2 \end{aligned} \quad (46)$$

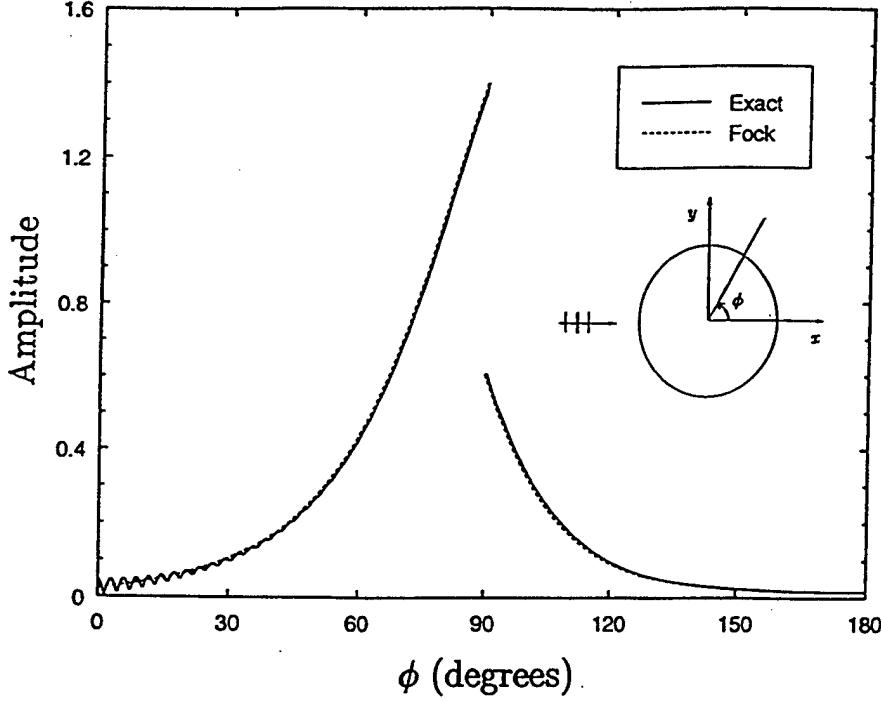


Figure 2: Amplitude of $K_\phi^{TE,NU}(a, \phi, z)$ for circular cylinder, $ka = 60$, $\phi^i = 180^\circ$, $\theta^i = 90^\circ$.

while for the shadow region (21) yields

$$\mathbf{K}^{TE}(a, \phi, z) \approx \left[-\hat{\phi} \sin \theta^i \pm \hat{z} \cos \theta^i \right] e^{ika \sin \theta^i |\phi^i \pm \pi/2 - \phi|} e^{-ikz \cos \theta^i} \cdot g \left[\left(\frac{ka \sin \theta^i}{2} \right)^{1/3} |\phi^i \pm \pi/2 - \phi| \right], \quad \pi/2 \leq |\phi - \phi^i| \leq \pi \quad (47)$$

where the \pm corresponds to the shadow boundary at $\phi^i \pm \pi/2$, respectively. For illumination by the TM plane wave given by (25) and (26), for the illuminated region we obtain from (35)

$$\mathbf{K}^{TM,NU}(a, \phi, z) \approx i\hat{z}Y_0 e^{-ika \sin \theta^i \cos(\phi - \phi^i)} e^{-ikz \cos \theta^i} \frac{\tilde{F} \left[- \left(\frac{1}{2}ka \sin \theta^i \right)^{1/3} \cos(\phi - \phi^i) \right]}{\left(\frac{1}{2}ka \sin \theta^i \right)^{1/3}} \quad |\phi - \phi^i| \leq \pi/2 \quad (48)$$

while for the shadow region (42) yields

$$K_z^{TM}(a, \phi, z) \approx iY_0 e^{ika \sin \theta^i |\phi^i \pm \pi/2 - \phi|} e^{-ikz \cos \theta^i} \frac{f \left[\left(\frac{1}{2}ka \sin \theta^i \right)^{1/3} |\phi^i \pm \pi/2 - \phi| \right]}{\left(\frac{1}{2}ka \sin \theta^i \right)^{1/3}} \quad \pi/2 \leq |\phi - \phi^i| \leq \pi. \quad (49)$$

In Figure 2 we have plotted the amplitude of the approximate TE NU current, $K_\phi^{TE,NU}(a, \phi, z)$, for a circular cylinder with $ka = 60$ obtained from (46) and (47) with $\phi^i = 180^\circ$ and $\theta^i = 90^\circ$ (normal incidence) along with the amplitude of the exact current obtained from the

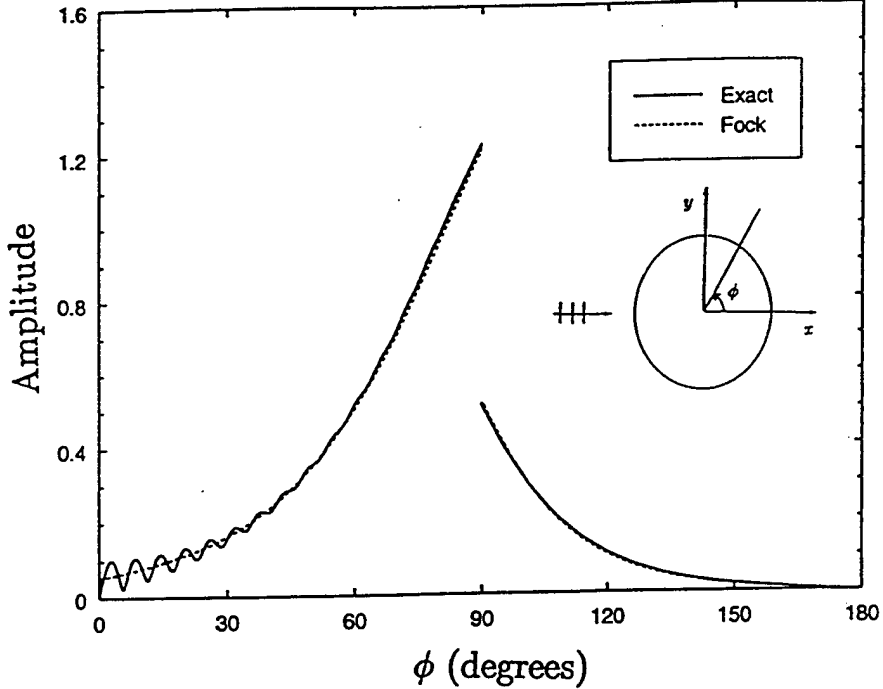


Figure 3: Amplitude of $K_z^{TE,NU}(a, \phi, z)$ for a circular cylinder, $ka = 60$, $\phi^i = 180^\circ$, $\theta^i = 30^\circ$.

eigenfunction expansion for scattering from a circular cylinder. The amplitude is discontinuous at the shadow boundary at $\phi = 90^\circ$ because the TE PO current is discontinuous there, and hence when subtracted from the continuous total current gives a discontinuous NU current. The approximate current is seen to closely fit the exact current except for the ripple behavior of the exact current in the deep shadow region in the vicinity of $\phi = 0^\circ$. This ripple behavior is the result of interference between the dominant creeping waves launched at $\phi = \pm 90^\circ$ both of which are present in the exact eigenfunction expansion of the current, whereas the approximate current in the range $0^\circ \leq \phi \leq 180^\circ$ contains only the dominant creeping wave launched at $\phi = 90^\circ$. Much the same remarks apply to the comparison of the plots in Figure 3 of the approximate and exact z component of the TE NU current for oblique incidence ($\theta^i = 30^\circ$).

In Figure 4 we have plotted the amplitude of the approximate TM NU current, $K_z^{TM,NU}(a, \phi, z)$, obtained from (48) and (49) for normal incidence, along with the amplitude of the exact current. Here there is no discontinuity at the shadow boundary because the TM PO current is zero in the illuminated region at the shadow boundary. The approximate current closely matches the exact current everywhere. No ripple behavior is observed here for the exact current because the creeping waves attenuate much more rapidly for TM than for TE illumination.

Next we consider the parabolic cylinder with focal length h . The currents are given in terms of the parabolic cylindrical coordinates (ξ, η, z) discussed in [17, ch. 7]. The surface of the scattering cylinder is given by $\eta = \eta_1 = \sqrt{2h}$. The derivations of the Fock currents are straightforward but somewhat lengthy. Expressions given in [17, ch. 7] are used, as well as the formula $\rho_n = (\xi^2 + \eta_1^2)^{3/2}/\eta_1$ for the radius of curvature of a parabolic cylinder in the plane normal to the z -axis. We give only the results here. For illumination by the TE plane wave given by (1) and (2) with $0 < \phi^i < \pi$, we obtain from (11) the Fock approximation for the NU current

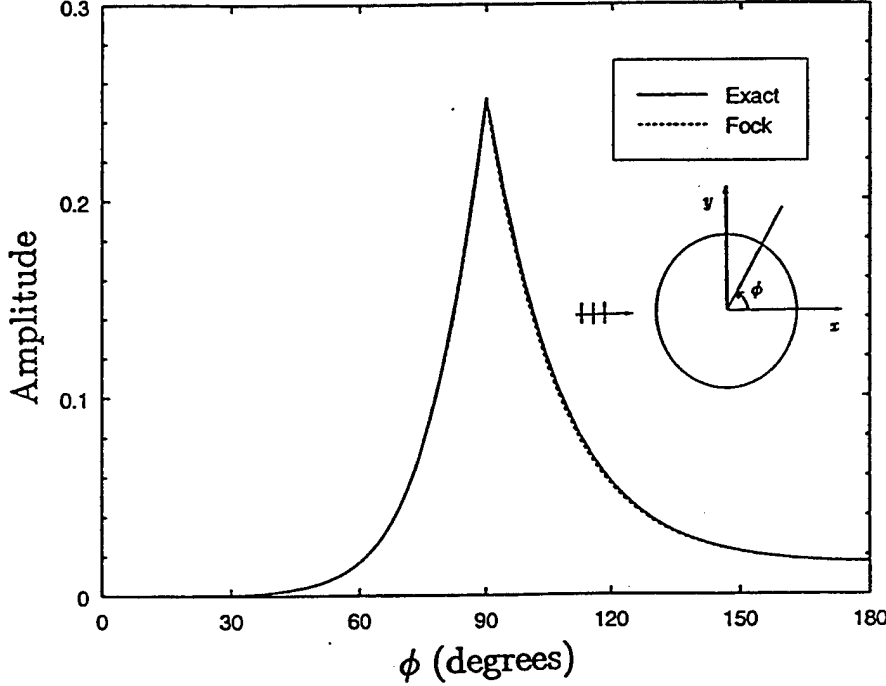


Figure 4: Amplitude of $K_z^{TM,NU}(a, \phi, z)$ for a circular cylinder, $ka = 60$, $\phi^i = 180^\circ$, $\theta^i = 90^\circ$.

in the illuminated region

$$\mathbf{K}^{TE,NU}(\xi, \eta_1, z) \approx \left[\hat{\xi} \sin \theta^i + \hat{z} \cos \theta^i \frac{\xi \cos \phi^i + \eta_1 \sin \phi^i}{(\xi^2 + \eta_1^2)^{1/2}} \right] e^{-ikh \sin \theta^i \left(\cos \phi^i \frac{\xi^2 - \eta_1^2}{\eta_1^2} + 2 \sin \phi^i \frac{\xi}{\eta_1} \right)} \cdot e^{-ikz \cos \theta^i} \tilde{G} \left[(kh \sin \theta^i)^{1/3} \frac{\eta_1 \cos \phi^i - \xi \sin \phi^i}{\eta_1} \right], \quad \xi > \eta_1 \cot \phi^i. \quad (50)$$

For the shadow region, (21) yields

$$\mathbf{K}^{TE}(\xi, \eta_1, z) \approx \left[\hat{\xi} \sin \theta^i + \hat{z} \cos \theta^i \right] e^{ikh \sin \theta^i \left[\ln \left(\eta_1^{-1} (-\xi + \sqrt{\xi^2 + \eta_1^2} \cot(\phi^i/2)) \right) - \xi \eta_1^{-2} \sqrt{\xi^2 + \eta_1^2} \right]} e^{-ikz \cos \theta^i} \cdot g \left[(kh \sin \theta^i)^{1/3} \ln \left(\eta_1^{-1} (-\xi + \sqrt{\xi^2 + \eta_1^2} \cot \phi^i) \right) \right] \frac{1}{\sqrt{\sin \phi^i}} \left(\frac{\eta_1^2}{\xi^2 + \eta_1^2} \right)^{1/4}, \quad \xi \leq \eta_1 \cot \phi^i. \quad (51)$$

It can be convenient to replace the variable ξ which ranges from $-\infty$ to $+\infty$ with a generalized angle variable ϕ_g (not to be confused with the polar angle ϕ) defined by $\phi_g = \tan^{-1}(\xi/\eta_1)$ (or $\xi = \eta_1 \tan \phi_g$) which ranges from $-\pi/2$ to $\pi/2$ with the shadow boundary given by $\phi_{g,SB} = \pi/2 - \phi^i$. In terms of ϕ_g (50) and (51) become

$$\mathbf{K}^{TE,NU}(\phi_g, kh, z) \approx \left[\hat{\xi} \sin \theta^i + \hat{z} \cos \theta^i \right] \cos \phi_g (\sin \phi^i + \cos \phi^i \tan \phi_g) \cdot e^{-ikh \sin \theta^i (\cos \phi^i (\tan^2 \phi_g - 1) + 2 \sin \phi^i \tan \phi_g)} e^{-ikz \cos \theta^i} \tilde{G} \left[(kh \sin \theta^i)^{1/3} (\cos \phi^i - \sin \phi^i \tan \phi_g) \right], \quad \phi_g > \pi/2 - \phi^i \quad (52)$$

and

$$\mathbf{K}^{TE}(\phi_g, kh, z) \approx \left[\hat{\xi} \sin \theta^i + \hat{z} \cos \theta^i \right] e^{ikh \sin \theta^i \left\{ \ln [(-\tan \phi_g + |\cos \phi_g|^{-1}) \cot(\phi^i/2)] - \tan \phi_g |\cos \phi_g|^{-1} \right\}}$$

$$\cdot e^{-ikz \cos \theta^i} g \left[(kh \sin \theta^i)^{1/3} \ln \left[(-\tan \phi_g + |\cos \phi_g|^{-1}) \cot \phi^i \right] \right] \frac{|\cos \phi_g|^{1/2}}{\sqrt{\sin \phi^i}}, \\ \phi_g \leq \pi/2 - \phi^i. \quad (53)$$

For illumination by the TM plane wave given by (25) and (26), in the illuminated region we obtain from (35) or (36)

$$K_z^{TM,NU}(\xi, \eta_1, z) \approx iY_0 \frac{\eta_1}{(\xi^2 + \eta_1^2)^{1/2}} e^{-ikh \sin \theta^i \left(\cos \phi^i \frac{\xi^2 - \eta_1^2}{\eta_1^2} + 2 \sin \phi^i \frac{\xi}{\eta_1} \right)} \\ \cdot e^{-ikz \cos \theta^i} \frac{\tilde{F} \left[(kh \sin \theta^i)^{1/3} \eta_1^{-1} (\eta_1 \cos \phi^i - \xi \sin \phi^i) \right]}{(kh \cos \theta^i)^{1/3}}, \quad \xi \geq \eta_1 \cot \phi^i \quad (54)$$

while in the shadow region we obtain from (42)

$$K_z^{TM}(\xi, \eta_1, z) \approx iY_0 e^{ikh \sin \theta^i \left[\ln \left(\eta_1^{-1} (-\xi + \sqrt{\xi^2 + \eta_1^2} \cot(\phi^i/2)) \right) - \xi \eta_1^{-2} \sqrt{\xi^2 + \eta_1^2} \right]} e^{-ikz \cos \theta^i} \\ \cdot \frac{f \left[(kh \sin \theta^i)^{1/3} \ln \left(\eta_1^{-1} (-\xi + \sqrt{\xi^2 + \eta_1^2} \cot \phi^i) \right) \right]}{\sqrt{\sin \phi^i} (kh \sin \theta^i)^{1/3}} \left(\frac{\eta_1^2}{\xi^2 + \eta_1^2} \right)^{3/4}, \quad \xi \leq \eta_1 \cot \phi^i. \quad (55)$$

In terms of the generalized angle variable ϕ_g , these expressions are respectively

$$K_z^{TM,NU}(\phi_g, kh, z) \approx iY_0 |\cos \phi_g| e^{-ikh \sin \theta^i [\cos \phi^i (\tan^2 - 1) + 2 \sin \phi^i \tan \phi_g]} e^{-ikz \cos \theta^i} \\ \cdot \frac{\tilde{F} \left[(kh \sin \theta^i)^{1/3} (\cos \phi^i - \sin \phi^i \tan \phi_g) \right]}{(kh \sin \theta^i)^{1/3}}, \quad \phi_g \geq \pi/2 - \phi^i \quad (56)$$

and

$$K_z^{TM}(\phi_g, kh, z) \approx iY_0 e^{ikh \sin \theta^i \left\{ \ln [(-\tan \phi_g + |\cos \phi_g|^{-1}) \cot(\phi^i/2)] - \tan \phi_g |\cos \phi_g|^{-1} \right\}} \\ \cdot e^{-ikz \cos \theta^i} \frac{f \left[(kh \sin \theta^i)^{1/3} \ln [(-\tan \phi_g + |\cos \phi_g|^{-1}) \cot \phi^i] \right]}{\sqrt{\sin \phi^i} (kh \sin \theta^i)^{1/3}}, \quad \phi_g \leq \pi/2 - \phi^i. \quad (57)$$

In Figure 5 we show plots of the approximate TE NU current $K_\xi^{TE,NU}(\phi_g, kh, z)$ for a parabolic cylinder with $kh = 60$, obtained from (52) and (53) with $\phi^i = 30^\circ$ and $\theta^i = 90^\circ$ (normal incidence). Also plotted is the exact current obtained from [17, Eq.(7.47)] using expansions given in [18] and [19]. The approximation, while not quite as good as for the circular cylinder, is still very close.

In Figure 6 we show a comparison of the z component of the approximate TE NU current for the same parabolic cylinder with $\phi^i = 30^\circ$ and $\theta^i = 30^\circ$ (oblique incidence), and the exact current obtained from [17, Eq.(7.47)] together with [13], [18], and [19]. Again the approximation is quite good throughout the range.

Plots of the approximate TM NU current $K_z^{TM,NU}(\phi_g, kh, z)$ obtained from (56) and (57) for normal incidence and of the corresponding exact current obtained from [17, Eq.(7.12)] and [18]

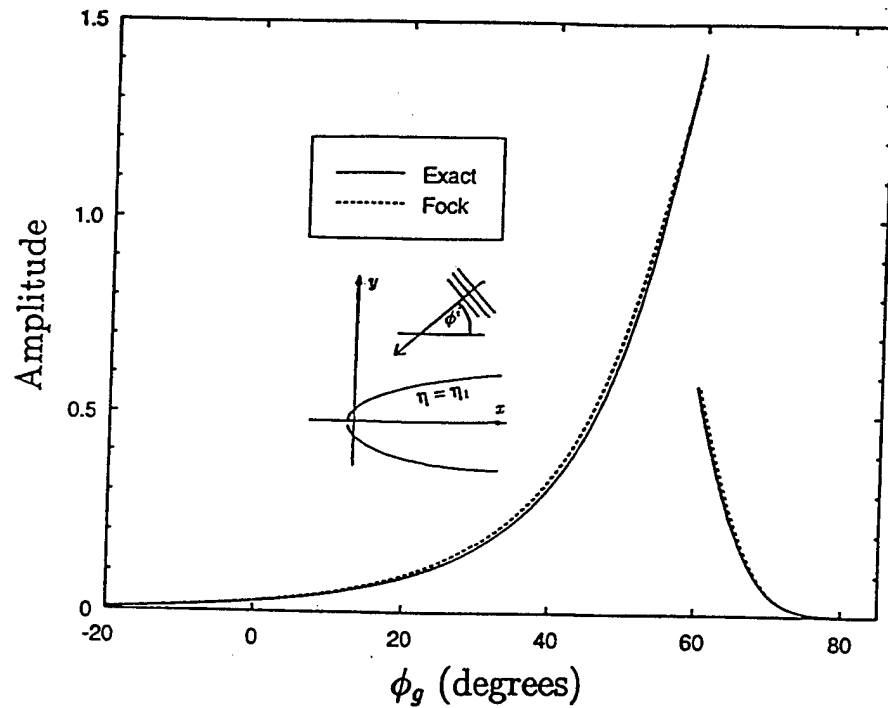


Figure 5: Amplitude of $K_{\xi}^{TE,NU}(\phi_g, kh, z)$ for a parabolic cylinder, $kh = 60$, $\phi^i = 30^\circ$, $\theta^i = 90^\circ$.

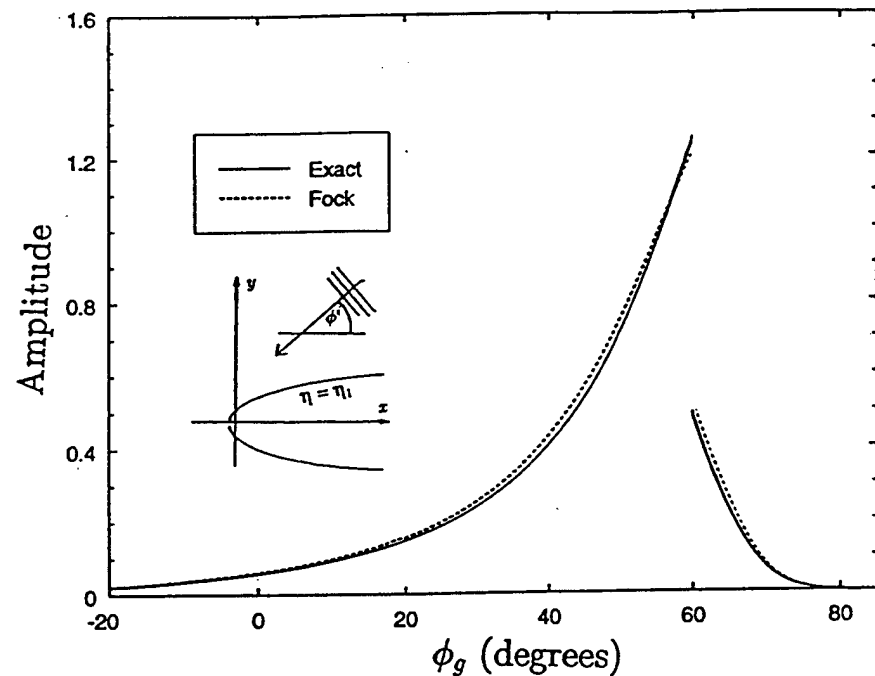


Figure 6: Amplitude of $K_z^{TE,NU}(\phi_g, kh, z)$ for a parabolic cylinder, $kh = 60$, $\phi^i = 30^\circ$, $\theta^i = 30^\circ$.

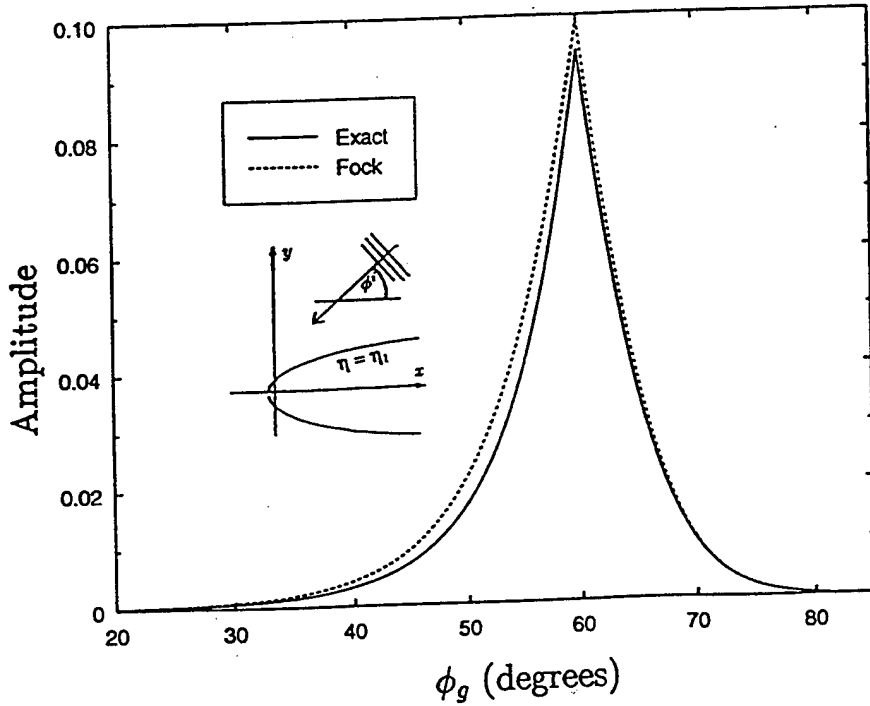


Figure 7: Amplitude of $K_{\xi}^{TM,NU}(\phi_g, kh, z)$ for a parabolic cylinder, $kh = 60$, $\phi^i = 30^\circ$, $\theta^i = 90^\circ$.

are displayed in Figure 7. Here the approximation, while acceptable, differs somewhat from the exact current especially in the shadow region, primarily because the value of the TM current at the shadow boundary $\phi_g = 60^\circ$ is significantly less than the exact value. The reason for this discrepancy is that the Fock current approximation is derived under the assumption that the derivative of the radius of curvature at the shadow boundary is equal to zero, a condition satisfied by the circular cylinder but not by the parabolic cylinder except when the shadow boundary is at the vertex of the parabolic cylinder. The discrepancy between the exact and approximate values at the shadow boundary of the parabolic cylinder is present in Figures 5 and 6 as well, but to a lesser degree.

3 Integrating the Fock Currents to Obtain ILDC's

We will now show how the ILDC's corresponding to the Fock currents presented in Section 2 can be obtained efficiently. The ILDC's for the shadow boundary of a convex cylinder represent the fields radiated by the nonuniform Fock currents on that cylinder. Specifically, the far field radiated by a strip of thickness dz' , which is described by the curve C on the cylinder, is given by

$$d\mathbf{E}^{NU}(\mathbf{r}) \xrightarrow{r \rightarrow \infty} \frac{dz' ik e^{ikr}}{4\pi r} \sqrt{\frac{\mu}{\epsilon}} \int_C e^{-ik\hat{\mathbf{r}} \cdot \mathbf{r}_C(s)} [\mathbf{K}^{NU}(\theta^i, \phi^i, s) - \hat{\mathbf{r}} \hat{\mathbf{r}} \cdot \mathbf{K}^{NU}(\theta^i, \phi^i, s)] ds, \quad (58)$$

where $\hat{\mathbf{r}}$ is the direction to the far-field observation point, $\mathbf{r}_C(s)$ is the parametric representation of C , and \mathbf{K}^{NU} is the nonuniform Fock current. In the illuminated region, the curve C is normal to the shadow boundary. In the shadow region, C is the geodesic whose angle with the axial direction is θ^i , as shown in Figure 1.

In general it is not possible to evaluate the integral (58) in closed form. However, as we will now demonstrate, an accurate and rapidly calculable approximation to this integral can be obtained.

3.1 Quadratic Polynomial Approximations of the Amplitude and Phase of the ILDC Radiation Integral

Begin by considering one of the components of the electric field $d\mathbf{E}$ in (58) and write this component as

$$dE(\mathbf{r}) = \int_{s_a}^{s_b} A(s) e^{-iP(s)} ds, \quad (59)$$

where the amplitude $A(s)$ and the phase $P(s)$ are functions of the angles of incidence and observation. The amplitude and phase functions are determined from the nonuniform current and the far-field Green's function occurring in (58). For convenience, we allow the amplitude $A(s)$ to be complex. Moreover, the expressions in Section 2 for the Fock currents and the factor $e^{-ik\hat{\mathbf{r}} \cdot \mathbf{r}_C(s)}$ determine the unwrapped phase of the integrand, so that the function $P(s)$ is continuous except possibly at the shadow boundary. Thus, the phase function $P(s)$ is *not* restricted to a finite interval of length 2π .

We can divide the integration in (59) into subintervals and have

$$\int_{s_a}^{s_b} A(s) e^{-iP(s)} ds = \sum_{j=1}^n \int_{s_j}^{s_{j+1}} A(s) e^{-iP(s)} ds \quad (60)$$

where $s_1 = s_a$, $s_{n+1} = s_b$, and $s_j < s_{j+1}$. The form of the functions $A(s)$ and $P(s)$ leads one to assume that these functions can be accurately approximated by quadratic polynomials of s in each of the intervals $s_j < s < s_{j+1}$ when these intervals are chosen appropriately. Hence,

$$\int_{s_j}^{s_{j+1}} A(s) e^{-iP(s)} ds \simeq \int_{s_j}^{s_{j+1}} (c_0 s^2 + c_1 s + c_2) e^{-i(c_3 s^2 + c_4 s + c_5)} ds \quad (61)$$

where c_0 , c_1 , c_2 , c_3 , c_4 , and c_5 are constants independent of s .

These constants will be determined such that the quadratic polynomials fit A and P at the endpoints s_j and s_{j+1} and at the midpoint $s_{j+1/2} = (s_j + s_{j+1})/2$:

$$A(s) = c_0 s^2 + c_1 s + c_2, \quad \text{for } s = s_j, s = s_{j+1/2}, s = s_{j+1}, \quad (62)$$

which gives

$$c_0 = 2(s_{j+1} + s_j) \frac{A(s_{j+1}) - A(s_j)}{(s_{j+1} - s_j)^3} + 4 \frac{s_{j+1} A(s_{j+1}) - s_j A(s_j)}{(s_{j+1} - s_j)^3} - 4 \frac{A(s_{j+1/2})}{(s_{j+1} - s_j)^2}, \quad (63)$$

$$c_1 = \frac{A(s_{j+1}) - A(s_j)}{s_{j+1} - s_j} - c_0(s_{j+1} + s_j), \quad (64)$$

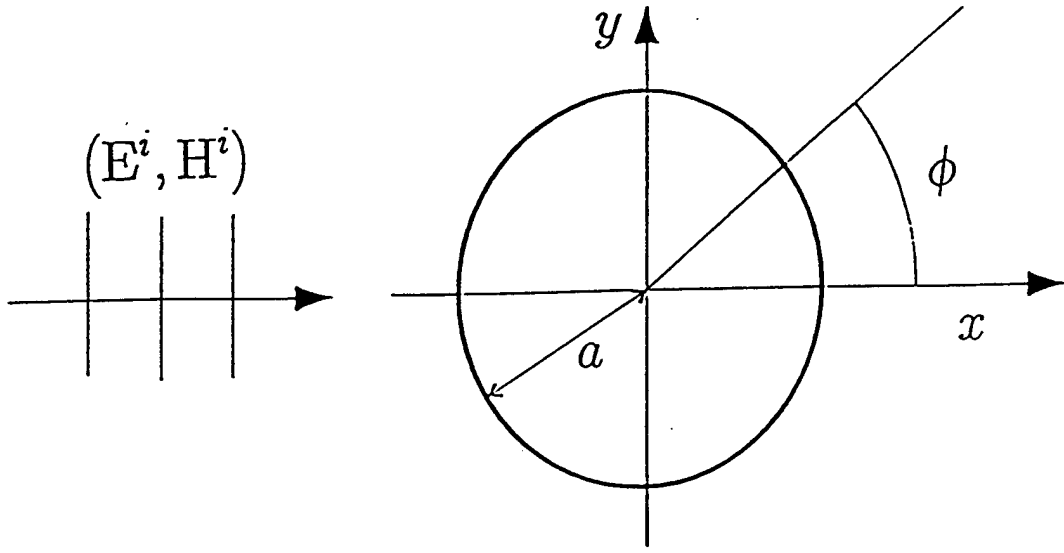


Figure 8: Circular cylinder illuminated by a TE plane wave

and

$$c_2 = \frac{s_{j+1}A(s_j) - s_jA(s_{j+1})}{s_{j+1} - s_j} + c_0s_j s_{j+1}. \quad (65)$$

Similarly,

$$P(s) = c_3s^2 + c_4s + c_5, \quad \text{for } s = s_j, s = s_{j+1/2}, s = s_{j+1} \quad (66)$$

and we find that c_3 , c_4 , and c_5 are given by (63), (64), and (65), respectively, with A replaced by P . These expressions for the constants c_0 , c_1 , c_2 , c_3 , c_4 , and c_5 are well behaved for all functions A and P that are continuous in the interval $s_j < s < s_{j+1}$. In principle we could let $P(s)$ be continuous for all s except at the shadow boundary. However, in practical calculations we permit $P(s)$ to have discontinuities that are multiples of 2π at the points s_j .

In the appendix we have shown how the integral on the right side of (61) can be evaluated in closed form in terms of the Fresnel function. Thus the ILDC's are expressed as a finite summation involving the Fresnel function and the values of the amplitude and the unwrapped phase of the integrand in (58) evaluated at the points s_j .

3.2 Numerical Verification of the Quadratic Approximations

We will now use a numerical example to verify the quadratic approximation of the phase and amplitude in (61). We consider the far field radiated by the NU current on the circular cylinder shown in Figure 8. The incident field is a plane TE wave with $H_z^i = e^{ikx}$, and only the NU current in the angular region $0 \leq \phi \leq \pi$ will be taken into account. The magnetic far field for this NU current can be written as $H_z^{NU,TE}(\mathbf{r}) = \mathcal{F}^{NU,TE}(\phi)e^{ikr}/\sqrt{kr}$, where the far-field pattern is given by

$$\mathcal{F}^{NU,TE}(\phi) = \int_{s_a}^{s_b} A(s)e^{-iP(s)}ds, \quad (67)$$

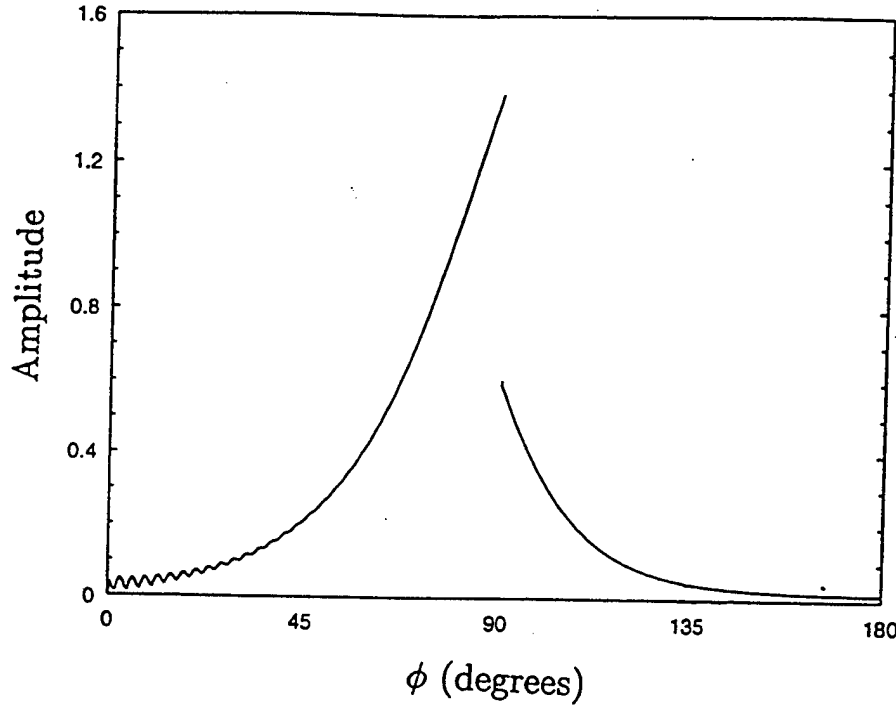


Figure 9: Amplitude of the exact nonuniform TE current on circular cylinder for $ka = 60$.

with $s_a = 0$, $s_b = \pi$,

$$A(s) = -\frac{ka}{\sqrt{8\pi}} |K_{\phi}^{NU,TE}(s)| \cos(\phi - s), \quad (68)$$

and

$$P(s) = ka \cos(\phi - s) - \text{Phase}(K_{\phi}^{NU,TE}(s)) \quad (69)$$

where $\text{Phase}(K_{\phi}^{NU,TE}(s))$ is continuous (i.e., *not* modulo 2π) apart from the discontinuity at the shadow boundary.

The amplitude and unwrapped phase of NU current are shown in Figure 9 and 10, respectively, for $ka = 60$. Notice that both the unwrapped phase and the amplitude of the NU current have discontinuities at the shadow boundary, and that the unwrapped phase is almost linear on the shadow side.

Figures 11-14 show the exact values and the quadratic approximations of $A(s)$ and $P(s)$ for $\phi = 0^\circ$ and $\phi = 90^\circ$. The number of segments n in (60) is 6 and $s_j = \pi(j-1)/6$, so the shadow region $0 \leq s < \pi/2$, as well as the illuminated region $\pi/2 \leq s \leq \pi$, are divided into three subregions. Thus, the length of the subintervals is 5λ . To better illustrate the accuracy of the quadratic phase approximation, we have introduced discontinuities in the phase at the endpoints s_j . We see that the quadratic phase approximation is excellent for both these angles of observation, but that the quadratic amplitude approximation deviates somewhat from the exact amplitude for $\phi = 0^\circ$.

The quadratic approximations can be improved by using unequal spacing with a greater density of points taken in the region of s that contributes most strongly to the far field at ϕ . As an example, this is done in Figures 15 and 16 for $\phi = 0^\circ$ where the endpoints are given by $s_1 = 0$, $s_2 = 60^\circ$, $s_3 = 80^\circ$, $s_4 = 90^\circ$, $s_5 = 105^\circ$, $s_6 = 135^\circ$, and $s_7 = 180^\circ$. The quadratic amplitude approximation is clearly better in Figure 15 than in Figure 11 with equal spacing.

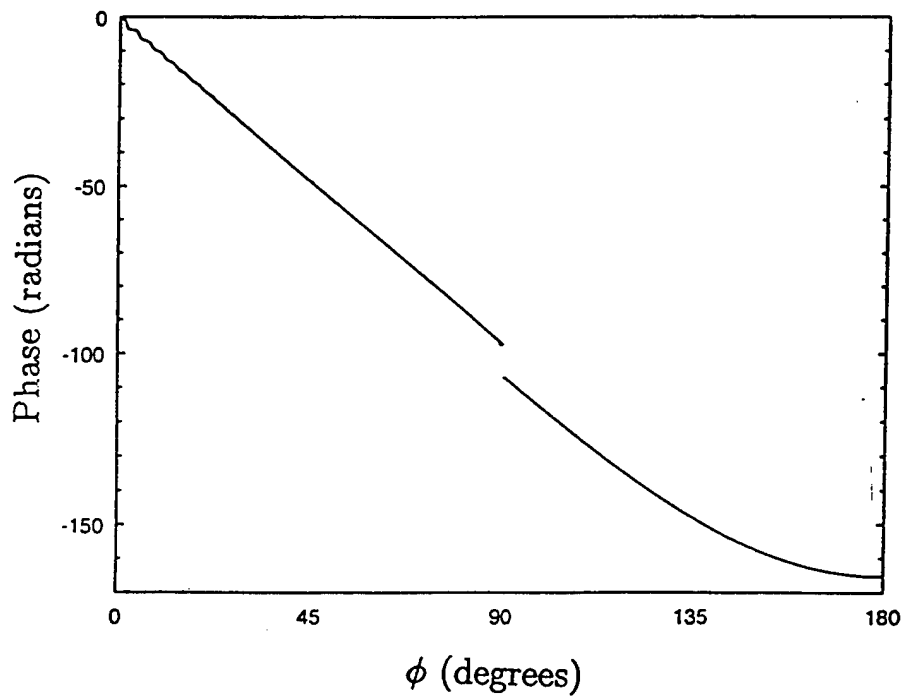


Figure 10: Phase of the exact nonuniform TE current on circular cylinder for $ka = 60$.

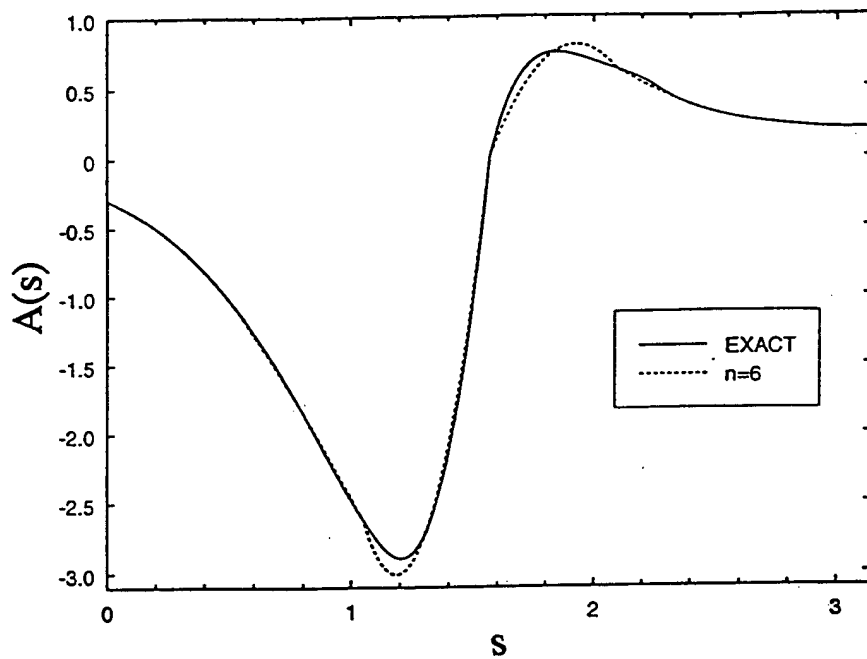


Figure 11: Exact values and quadratic approximation of $A(s)$ for $n = 6$, $\phi = 0^\circ$, and $ka = 60$. The endpoints are $s_j = \pi(j - 1)/6$.

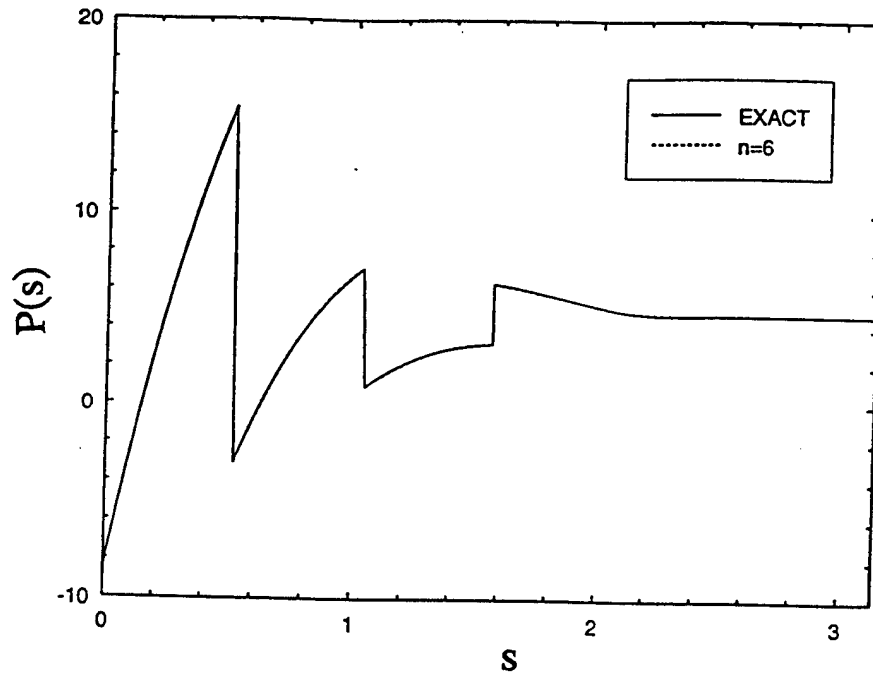


Figure 12: Exact values and quadratic approximation of $P(s)$ for $n = 6$, $\phi = 0^\circ$, and $ka = 60$. The endpoints are $s_j = \pi(j - 1)/6$.

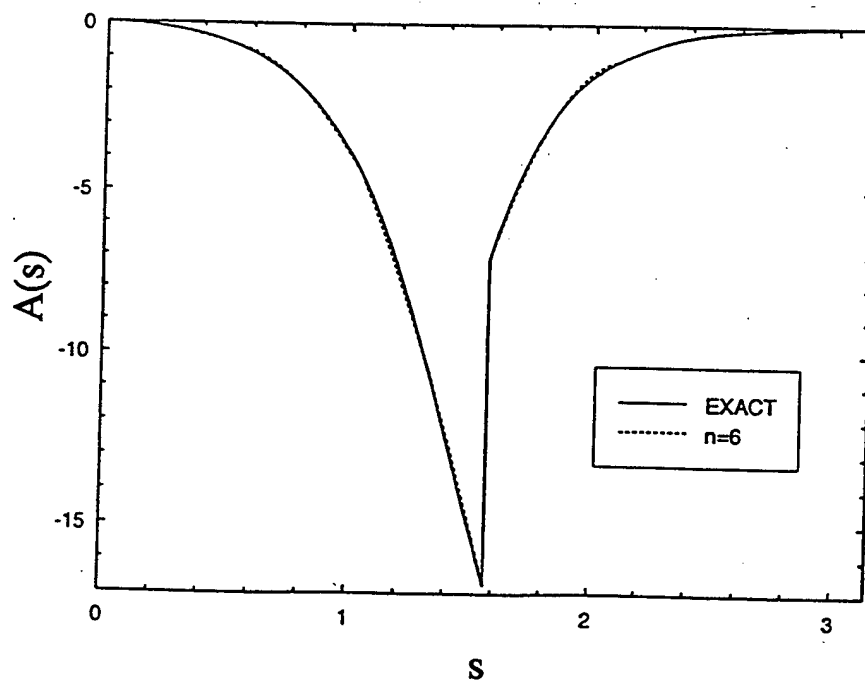


Figure 13: Exact values and quadratic approximation of $A(s)$ for $n = 6$, $\phi = 90^\circ$, and $ka = 60$. The endpoints are $s_j = \pi(j - 1)/6$.

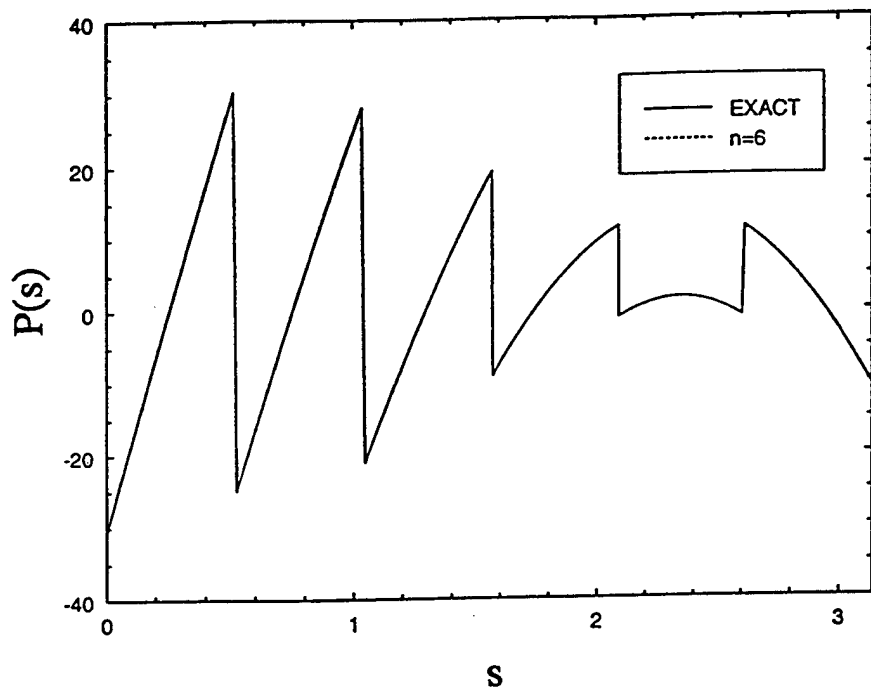


Figure 14: Exact values and quadratic approximation of $P(s)$ for $n = 6$, $\phi = 90^\circ$, and $ka = 60$. The endpoints are $s_j = \pi(j - 1)/6$.

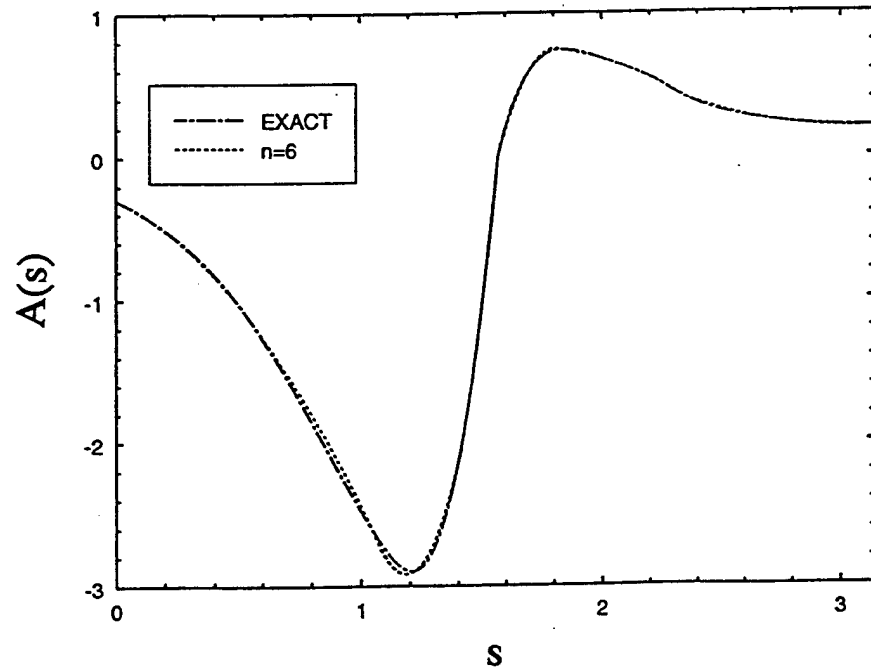


Figure 15: Exact values and quadratic approximation of $A(s)$ for $n = 6$, $\phi = 0^\circ$, and $ka = 60$. The endpoints are $s_1 = 0$, $s_2 = 60^\circ$, $s_3 = 80^\circ$, $s_4 = 90^\circ$, $s_5 = 105^\circ$, $s_6 = 135^\circ$, and $s_7 = 180^\circ$.

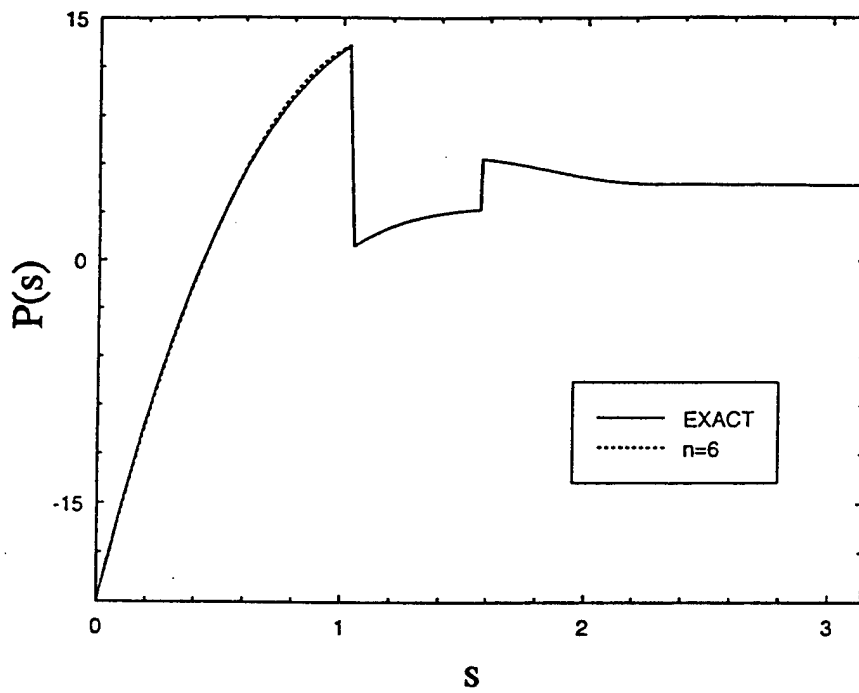


Figure 16: Exact values and quadratic approximation of $P(s)$ for $n = 6$, $\phi = 0^\circ$, and $ka = 60$. The endpoints are $s_1 = 0$, $s_2 = 60^\circ$, $s_3 = 80^\circ$, $s_4 = 90^\circ$, $s_5 = 105^\circ$, $s_6 = 135^\circ$, and $s_7 = 180^\circ$.

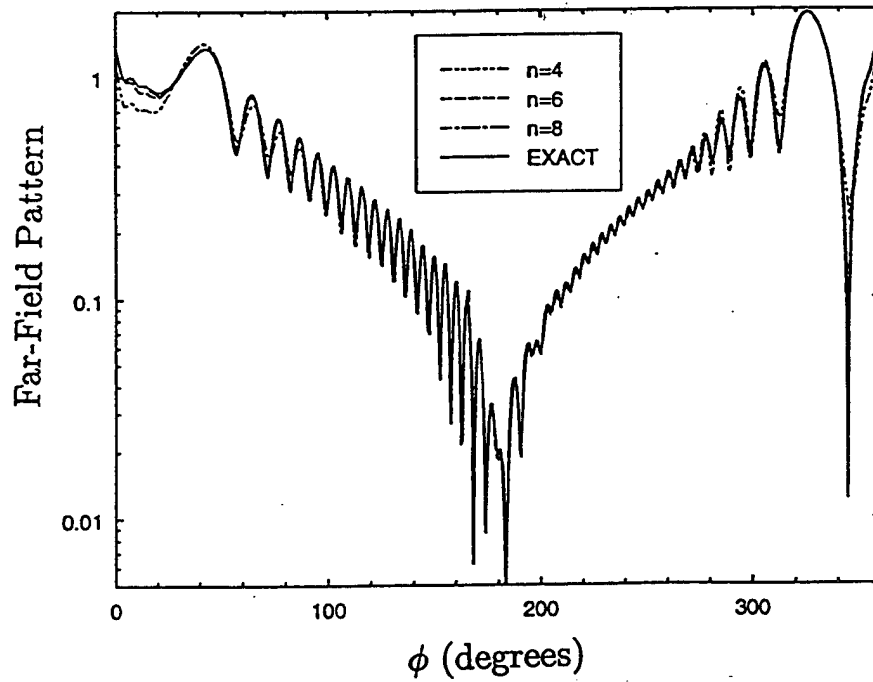


Figure 17: Exact and approximate NU TE far-field pattern for $ka = 60$ and $n = 4$, $n = 6$, and $n = 8$. The endpoints are $s_j = \pi(j - 1)/n$; $0^\circ \leq \phi \leq 360^\circ$.

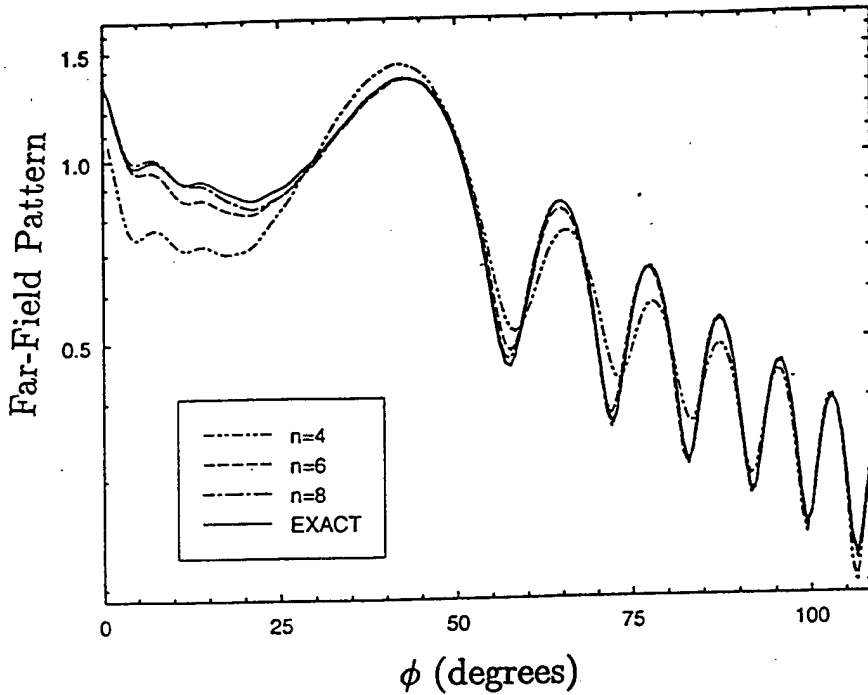


Figure 18: Exact and approximate NU TE far-field pattern for $ka = 60$ and $n = 4$, $n = 6$, and $n = 8$. The endpoints are $s_j = \pi(j - 1)/n$; $0^\circ \leq \phi \leq 110^\circ$.

Future work could determine the optimal set of endpoints s_j as a function of the far-field angle of observation. By making these endpoints depend on the far-field angle, one could probably increase the accuracy of the computed ILDC's and, at the same time, reduce the number of segments.

Having demonstrated the validity of the quadratic approximations for the amplitude $A(s)$ and phase $P(s)$, we can now calculate the far field that results from these approximations using (60) and (61). For the above example of a TE plane wave incident on a circular cylinder, the NU far-field pattern is shown in Figures 17 and 18. In these figures, the exact NU far-field pattern is shown together with the NU far-field patterns obtained using $n = 4$, $n = 6$, and $n = 8$ integration subintervals. The exact far-field pattern in these figures is obtained by numerically integrating the NU current shown in Figures 9 and 10.

Let us compare the far-field patterns obtained when the number of segments are $n = 4$, $n = 6$, and $n = 8$, and the endpoints are given by $s_j = \pi(j - 1)/n$. We notice that, except in the region around $\phi = 20^\circ$, the results obtained with $n = 4$ are very accurate. It is almost impossible to distinguish the exact result from the result obtained with $n = 8$, and we conclude that for $ka = 60$ it is sufficient to use $n = 6$ equally spaced endpoints.

The numerical examples in this section show that with the integration technique presented in Section 3.1, one can accurately compute the radiated fields using segments as large as 5λ . This is a significant improvement over standard current integrations that usually use segments of the order of $\lambda/6$.

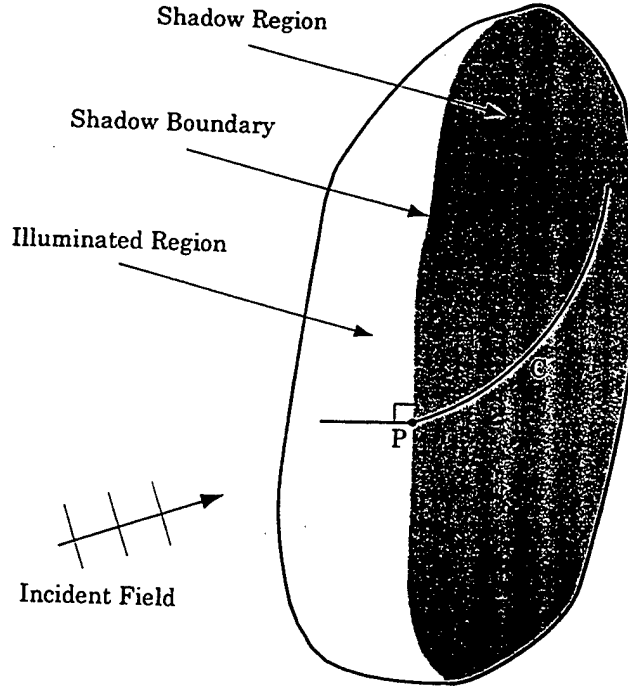


Figure 19: Three dimensional scatterer illuminated by a plane wave.

4 The Use of the ILDC's for a 3D Scatterer

In this section we show how the ILDC's for a convex cylinder are applied to calculate the scattered far field of a 3D scatterer. In applications the PO field will generally be known, and what is desired is the scattered field due to the NU currents on the 3D scatterer in the vicinity of its shadow boundary. The total scattered field is then obtained by adding the NU scattered field to the PO field. Consider a 3D scatterer with a smoothly varying radius of curvature illuminated by a plane wave (see Figure 19). The illuminated and shadowed portions of the surface are separated by the shadow boundary curve on the surface of the scatterer. Consider a point P on the shadow boundary and generate a curve C on the surface of the scatterer through P motivated by the behavior of the currents on the surface. In the shadow region, C is the geodesic emanating from P in the direction of the illuminating plane wave – the curve followed by the currents – while in the illuminated region where the currents are determined locally, C is simply the intersection of the surface with the plane through P perpendicular to the shadow boundary. A 2D convex cylindrical (in general not circular-cylindrical) surface can then be generated by passing straight lines (generators) through each point on C parallel to the shadow boundary at P . Now generate a curve C' through P on the cylindrical surface in the same way that C was generated on the surface of the 3D scatterer. Assume that the radius of curvature of the 3D scatterer is large in the direction parallel to the shadow boundary at P for points on the geodesic part of C , especially in the vicinity of P . Then the geodesic portion of C in the vicinity of P will be closely approximated by the geodesic portion of C' (a generalized helical curve on the convex cylindrical surface making a constant angle with its generators), and the ILDC's of the cylindrical surface at P will be a good approximation to the fields radiated by the NU currents on a differential strip of the 3D scatterer's surface containing C . The procedure for obtaining the

ILDC's corresponding to the point P on the shadow boundary of the 3D scatterer is repeated for all points on the shadow boundary, and the ILDC's then integrated along the shadow boundary to obtain an approximation to the far field radiated by the NU currents on the 3D scatterer.

It should be noted that a creeping wave geodesic on the surface of the actual scatterer will in general diverge from the corresponding helical creeping wave geodesic on the approximating convex cylinder surface as the distance from the launching shadow boundary point increases. However the exponential decay of the creeping waves (see Eqs. (24) and (45)) insures that the major contribution to the diffracted far field comes from the current on the portion of the geodesic close to the shadow boundary. Here the generalized helical geodesic can be expected to be a good approximation to the actual creeping wave geodesic, especially, if as assumed, the radius of curvature of the actual 3D scatterer is large in the direction parallel to the shadow boundary for points on the geodesic close to the launching shadow boundary point. An important consequence of this concentration of the creeping wave current in the vicinity of the shadow boundary is that the major ILDC contribution to the far field is in the forward direction, since the field in this region can be viewed as due to the shedding of the creeping waves along rays tangential to the scatterer at points close to the shadow boundary.

4.1 Calculation of the Fields Scattered by a Sphere

As an application of the NU ILDC's for the shadow boundary of the PEC circular cylinder, we calculated the far field of a PEC sphere illuminated by a plane wave by adding the integral of the ILDC for a cylinder to the PO field of the sphere, and compared the result to the exact scattered far field of the sphere as obtained from the Mie series solution. The sphere, of radius a , is assumed centered at the origin of a Cartesian coordinate system and illuminated by a plane wave propagating from above in the negative z -direction. The shadow boundary of the sphere is thus a circle of radius a in the $z = 0$ plane. A circular cylinder of radius a , enclosing the sphere, whose axis lies in the plane $z = 0$, will be tangent to the sphere along the circle of radius a , normal to the cylinder axis, with its center at the origin. Hence, a strip of the sphere's surface of constant equal width on either side of the meridian defined by $\phi = \text{constant}$ coincides in the limit, as the width of the strip shrinks to zero, with an azimuthal differential strip of surface of the enclosing cylinder. As the cylinder is rotated around the z -axis the entire surface of the sphere is obtained. Thus the far field of the sphere can be obtained by adding the integral of the NU-current ILDC of the cylinder to the PO far field of the sphere, as the cylinder axis is rotated from $\phi = 0$ to $\phi = 2\pi$. (It should be noted that an error is introduced in this approximation procedure by the fact that the differential strips of cylinder surface overlap in the vicinity of the poles of the sphere as the cylinder is rotated. This overlap is concentrated in the "polar" regions of the sphere, however, and if the radius of the sphere is large the NU currents will decay rapidly away from the shadow boundary so that the error attributable to the overlap of the differential strips can be expected to be small.

In Figure 20 we show the scattered H-plane far field for a sphere of size $ka = 60$ illuminated by a plane wave obtained by the method of ILDC's, along with the exact field obtained from the Mie series. The back and forward scatter directions correspond to $\theta = 0^\circ$ and $\theta = 180^\circ$,

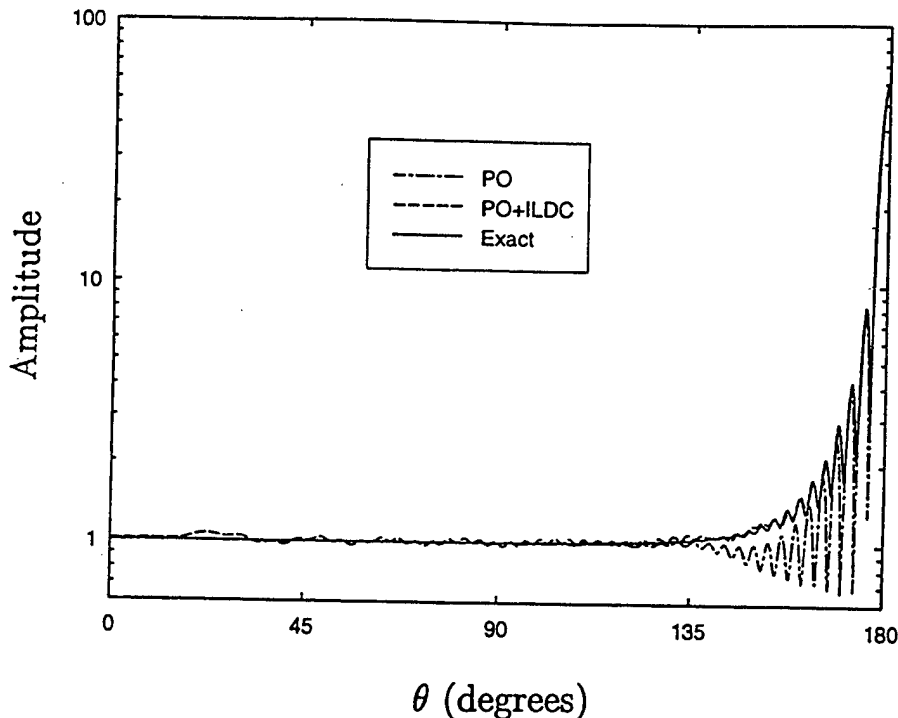


Figure 20: Amplitude of scattered H-plane far field of sphere, $ka = 60$, illuminated by a plane wave; $0^\circ \leq \theta \leq 180^\circ$.

respectively. The detail of Figure 20 for $130^\circ \leq \theta \leq 180^\circ$ is shown in Figure 21. It can be seen that a significant improvement upon the accuracy of the PO scattered field is obtained by adding the integral of the circular cylinder NU current ILDC to the PO field of the sphere. A similar result was obtained for the E-plane scattered far field pattern. Calculations for spheres smaller than $ka = 60$ have shown that the ILDC's significantly enhance the accuracy of the PO far field for spheres as small as $ka = 20$.

5 Conclusions

The nonuniform currents excited in the vicinity of the shadow boundary of a PEC object can contribute significantly to the total scattered far field of the object. The method of ILDC's is an important technique for calculating this NU far field which, added to the PO field, gives a considerably more accurate approximation to the total scattered far field than does the PO far field alone. The approach taken in this report to obtain ILDC's for the shadow boundary of a PEC 2D convex cylinder of general cross-section is to integrate the product of the free-space Green's function and the NU currents over a strip of surface of the 2D cylinder of differential width, transverse to the shadow boundary. Accurate and rapidly calculable Fock approximations to the NU currents are obtained and used. For circular and parabolic cylinders these NU current approximations are validated numerically. The integration required to obtain the ILDC's is itself performed rapidly by using quadratic polynomial approximations of both the amplitude and unwrapped phase of the integrand of the radiation integral, thereby enabling the integration to be performed in closed form involving Fresnel functions. Examples are given of the approximations of both the NU currents and the integrand of the radiation integral. As an application of this

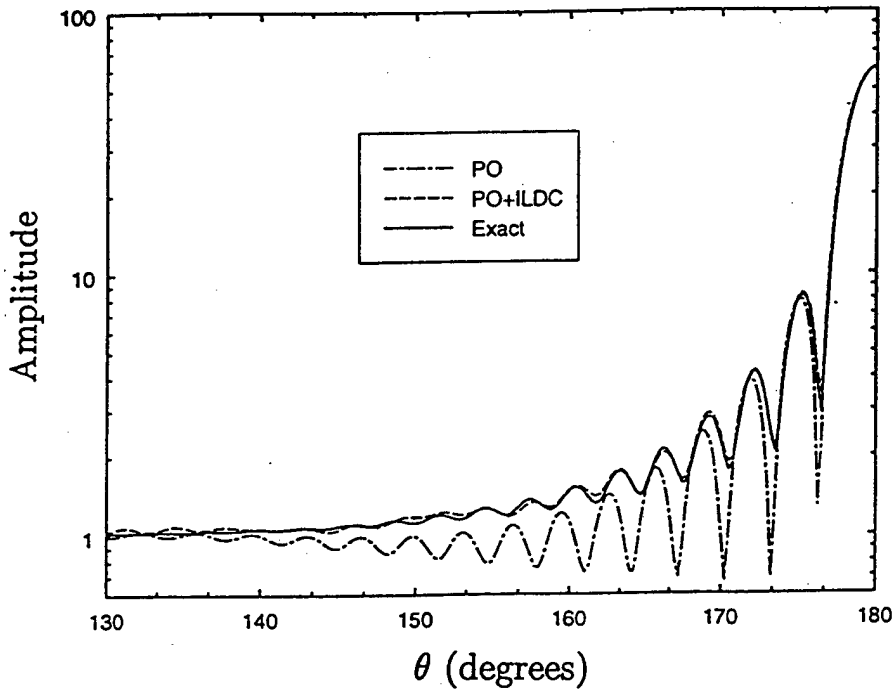


Figure 21: Amplitude of Scattered H-plane Far Field of Sphere, $ka = 60$, Illuminated by a Plane Wave; $130^\circ \leq \theta \leq 180^\circ$.

method of obtaining ILDC's for convex PEC cylinders, the ILDC's of a PEC circular cylinder are obtained and integrated over the shadow boundary of a PEC sphere illuminated by a plane wave to obtain the NU current far field. This field, added to the PO far field, is shown to considerably improve upon the accuracy of the PO approximation of the exact total scattered far field of the sphere.

References

- [1] Ufimtsev, P. Ya. (1962) *Method of Edge Waves in the Physical Theory of Diffraction*, Moscow: Sovyetskoye Radio. (Available in English from Nat. Tech. Inform. Serv., Springfield VA 22161, AD733203.)
- [2] Mitzner, K.M. (1974) *Incremental Length Diffraction Coefficients*, Tech. Rep. No. AFAL-TR-73-296, (Available from Nat. Tech. Inform. Serv., Springfield VA 22161, AD918861.)
- [3] Michaeli, A. (1984) "Equivalent edge currents for arbitrary aspects of observation," *IEEE Trans. Antenna. Propagat.*, **32**:252-258; and A. Michaeli, (1985) "Corrections to 'Equivalent edge currents for arbitrary aspects of observation,'" *IEEE Trans. Antenna. Propagat.*, **33**:227.
- [4] Knott, E.F. (1985) "The relationship between Mitzner's ILDC and Michaeli's equivalent currents," *IEEE Trans. Antenna. Propagat.*, **33**:112-114.
- [5] Shore, R.A., and Yaghjian, A.D. (1988) "Incremental diffraction coefficients for planar surfaces," *IEEE Trans. Antenna. Propagat.*, **36**:55-70; and Shore, R.A., and Yaghjian, A.D. (1989) "Corrections to 'Incremental diffraction coefficients for planar surfaces,'" *IEEE Trans. Antenna. Propagat.*, **37**:1342.
- [6] Hansen, T.B., and Shore, R.A. (1994) "Incremental length diffraction coefficients for the shadow boundary of a circular cylinder," *Proc. 1994 Progress in Electromagnetics Research Symposium (PIERS)*, European Space Agency, Noordwijk, The Netherlands, on CD-ROM.
- [7] Shore, R.A., and Hansen, T.B. (1995) "Incremental length diffraction coefficients for the shadow boundary of a parabolic cylinder," *Proc. 1995 Progress in Electromagnetics Research Symposium (PIERS)*, The University of Washington, Seattle, p. 1097.
- [8] Hansen, T.B., and Shore, R.A. (1996) "Incremental length diffraction coefficients for the shadow boundary of a general cylinder with smoothly varying radius of curvature," *Proc. 1996 Progress in Electromagnetics Research Symposium (PIERS)*, University of Innsbruck, Inst. of Meteorology and Geophysics, Austria, p. 499.
- [9] Yaghjian, A.D., Shore, R.A. and Woodworth, M.B. (1996) "Shadow boundary incremental length diffraction coefficients for perfectly conducting smooth, convex surfaces," *Radio Science*, **31**:1681-1695.
- [10] Hansen T.B., and Yaghjian, A.D. (1991) "Incremental diffraction coefficients for cylinders of arbitrary cross section: Application to diffraction from ridges and channels in perfectly conducting surfaces," *IEEE APS Symp. Digest*, The Univ. of Western Ontario, London Ontario, Canada:794-797.

- [11] Shore, R.A., and Yaghjian, A.D. (1998) "A comparison of two incremental diffraction coefficients for convex perfectly electrically conducting cylinders," *International Symposium on Electromagnetic Theory, International Union of Radio Science (URSI)*, Aristotle University of Thessaloniki, Thessaloniki Greece, May 1998.
- [12] Fock, V.A. (1965) *Electromagnetic Diffraction and Propagation Problems*, Oxford: Pergamon.
- [13] Hansen, T.B., and Shore, R.A. (1995) "The currents on a cylinder illuminated by a general plane wave," *IEEE Trans. Antenna. Propagat.*, **43**:1464-1465.
- [14] Bouche, D.P., Molinet, F.A., and Mittra, R. (1993) "Asymptotic and hybrid techniques for electromagnetic scattering," *Proceedings of IEEE*, **81**:1658-1684.
- [15] L.N. Medgyesi-Mitschang and D.L. Wang, "Hybrid solutions for scattering from perfectly conducting bodies of revolution" *IEEE Trans. Antennas Propagat.*, Vol. 31, pp. 570-583, July 1983.
- [16] G.T. Ruch, Ed., *Radar Cross Section Handbook*, New York: Plenum Press, 1970, Volume 1.
- [17] J.J. Bowman, T.B.A. Senior, and P.L.E. Uslenghi, (1969) *Electromagnetic and Acoustic Scattering by Simple Shapes*, Amsterdam: North-Holland Publishing Company. (A minus sign should be applied to the right-hand side of equations (7.12), (7.34), and (7.36).)
- [18] J.L. Blanchard and E.H. Newman, (1989) "Numerical Evaluation of Parabolic Cylinder Functions," *IEEE Trans. Antennas Propagat.*, **37**:519-523.
- [19] R.A. Shore and T.B. Hansen, (1996) "Numerical evaluation of the derivative of the parabolic cylinder function," *IEEE Trans. Antenna. Propagat.*, **44**:1300-1301.
- [20] M. Abramowitz and I.A. Stegun, (1972) *Handbook of Mathematical Functions*, New York: Dover, Ninth Printing.
- [21] Press, W.H., Teukolsky, S.A., Vetterling, W.T., and Flannery, B.P. (1992) *Numerical Recipes in Fortran*, New York: Oxford University Press.

Appendix

Closed-Form Expressions for an Integral

In this appendix we present closed-form expressions for the integral

$$I(c_0, c_1, c_2, c_3, c_4, c_5, a, b) = \int_a^b (c_0 s^2 + c_1 s + c_2) e^{-i(c_3 s^2 + c_4 s + c_5)} ds \quad (70)$$

occurring in the expression (61). We assume that c_0 , c_1 , and c_2 are complex and that c_3 , c_4 , c_5 , a , and b are real.

Case I: $c_3 > 0$

Integration by parts shows that

$$\begin{aligned} I(c_0, c_1, c_2, c_3, c_4, c_5, a, b) &= \frac{ic_0}{2c_3} \left[\left(b + \frac{c_4}{2c_3} \right) e^{-i(c_3 b^2 + c_4 b + c_5)} - \left(a + \frac{c_4}{2c_3} \right) e^{-i(c_3 a^2 + c_4 a + c_5)} \right] \\ &+ \frac{i}{2c_3} \left(c_1 - \frac{c_0 c_4}{c_3} \right) \left[e^{-i(c_3 b^2 + c_4 b + c_5)} - e^{-i(c_3 a^2 + c_4 a + c_5)} \right] \\ &+ \left(\frac{c_0}{2ic_3} - \frac{c_1 c_4}{2c_3} + c_2 + \frac{c_0 c_4^2}{4c_3^2} \right) \Lambda \end{aligned} \quad (71)$$

where

$$\Lambda = \sqrt{\frac{\pi}{2c_3}} e^{-i[c_5 - c_4^2/(4c_3)]} [\Omega(x_b) - \Omega(x_a)], \quad (72)$$

$$x_a = \sqrt{\frac{2c_3}{\pi}} \left\{ a + \frac{c_4}{2c_3} \right\}, \quad x_b = \sqrt{\frac{2c_3}{\pi}} \left\{ b + \frac{c_4}{2c_3} \right\}, \quad (73)$$

and

$$\Omega(x) = \int_0^x e^{-i\pi t^2/2} dt \quad (74)$$

is a Fresnel function. When $|x_a|$ and $|x_b|$ are large one can substitute the large-argument approximation for the Fresnel function [20, pp. 301-302]

$$\Omega(x) \sim \text{sign}(x) \frac{1-i}{2} + \left[\frac{i}{\pi x} - \frac{1}{\pi^2 x^3} - \frac{3i}{\pi^3 x^5} + O(x^{-7}) \right] e^{-i\pi x^2/2}, \quad |x| \rightarrow \infty \quad (75)$$

into (72) to get

$$\Lambda = \frac{i}{\sqrt{2\pi c_3}} \left[\left(\frac{1}{x_b} + \frac{i}{\pi x_b^3} - \frac{3}{\pi^2 x_b^5} \right) e^{-i(c_3 b^2 + c_4 b + c_5)} - \left(\frac{1}{x_a} + \frac{i}{\pi x_a^3} - \frac{3}{\pi^2 x_a^5} \right) e^{-i(c_3 a^2 + c_4 a + c_5)} \right]. \quad (76)$$

Numerical calculations show that it is advantageous to use (76) when $|x_a| > 10$ and $|x_b| > 10$. For $|x_a| \leq 10$ or $|x_b| \leq 10$, the routine “fresnel” of Numerical Recipes [21, pp. 248-250] can be used.

Case II: $c_3 < 0$

The integral can in this case be obtained from

$$I(c_0, c_1, c_2, c_3, c_4, c_5, a, b) = [I(c_0^*, c_1^*, c_2^*, -c_3, -c_4, -c_5, a, b)]^* \quad (77)$$

where $*$ indicates complex conjugation. The integral on the right side of (77) can be computed by the formulas given in Case I above.

Case III: $0 < |c_3| \ll 1$

In this case it is advantageous to obtain I from

$$I(c_0, c_1, c_2, c_3, c_4, c_5, a, b) = I(c_0, c_1, c_2, 0, c_4, c_5, a, b) + c_3 \frac{\partial I}{\partial c_3}(c_0, c_1, c_2, 0, c_4, c_5, a, b) \quad (78)$$

where

$$\frac{\partial I}{\partial c_3}(c_0, c_1, c_2, 0, c_4, c_5, a, b) = -i \int_a^b s^2(c_0 s^2 + c_1 s + c_2) e^{-i(c_4 s + c_5)} ds. \quad (79)$$

The integral can be easily evaluated in closed form by integrating by parts or, more simply, by using a symbolic-integration computer program.

Case IV: $c_3 = 0, c_4 \neq 0$

A straightforward calculation shows that

$$\begin{aligned} I(c_0, c_1, c_2, 0, c_4, c_5, a, b) &= \left[-\frac{c_0 b^2 + c_1 b + c_2}{i c_4} + \frac{2c_0 b + c_1}{c_4^2} + \frac{2c_0}{i c_4^3} \right] e^{-i(c_4 b + c_5)} \\ &- \left[-\frac{c_0 a^2 + c_1 a + c_2}{i c_4} + \frac{2c_0 a + c_1}{c_4^2} + \frac{2c_0}{i c_4^3} \right] e^{-i(c_4 a + c_5)}. \end{aligned} \quad (80)$$

Case V: $c_3 = 0, c_4 = 0$

A straightforward calculation shows that

$$I(c_0, c_1, c_2, 0, 0, c_5, a, b) = \left[\frac{1}{3} c_0 (b^3 - a^3) + \frac{1}{2} c_1 (b^2 - a^2) + c_2 (b - a) \right] e^{-i c_5}. \quad (81)$$

Equation (66) implies that the quantities $e^{-i(c_3 a^2 + c_4 a + c_5)}$ and $e^{-i(c_3 b^2 + c_4 b + c_5)}$, occurring in many of the expressions of this section, simply equal $e^{-iP(a)}$ and $e^{-iP(b)}$, respectively.

***MISSION
OF
ROME LABORATORY***

Mission. The mission of Rome Laboratory is to advance the science and technologies of command, control, communications and intelligence and to transition them into systems to meet customer needs. To achieve this, Rome Lab:

- a. Conducts vigorous research, development and test programs in all applicable technologies;
- b. Transitions technology to current and future systems to improve operational capability, readiness, and supportability;
- c. Provides a full range of technical support to Air Force Materiel Command product centers and other Air Force organizations;
- d. Promotes transfer of technology to the private sector;
- e. Maintains leading edge technological expertise in the areas of surveillance, communications, command and control, intelligence, reliability science, electro-magnetic technology, photonics, signal processing, and computational science.

The thrust areas of technical competence include: Surveillance, Communications, Command and Control, Intelligence, Signal Processing, Computer Science and Technology, Electromagnetic Technology, Photonics and Reliability Sciences.